

## The background in the $0\nu\beta\beta$ experiment GERDA

M. Agostini<sup>14</sup>, M. Allardt<sup>3</sup>, E. Andreotti<sup>5,17</sup>, A. M. Bakalyarov<sup>12</sup>, M. Balata<sup>1</sup>, I. Barabanov<sup>10</sup>, M. Barnabé Heider<sup>6,14,b</sup>, N. Barros<sup>3</sup>, L. Baudis<sup>18</sup>, C. Bauer<sup>6</sup>, N. Becerici-Schmidt<sup>13</sup>, E. Bellotti<sup>7,8</sup>, S. Belogurov<sup>10,11</sup>, S. T. Belyaev<sup>12</sup>, G. Benato<sup>18</sup>, A. Bettini<sup>15,16</sup>, L. Bezrukov<sup>10</sup>, T. Bode<sup>14</sup>, V. Brudanin<sup>4</sup>, R. Brugnera<sup>15,16</sup>, D. Budjás<sup>14</sup>, A. Caldwell<sup>13</sup>, C. Cattadori<sup>8</sup>, A. Chernogorov<sup>11</sup>, F. Cossavella<sup>13</sup>, E. V. Demidova<sup>11</sup>, A. Domula<sup>3</sup>, V. Egorov<sup>4</sup>, R. Falkenstein<sup>17</sup>, A. Ferella<sup>18,c</sup>, K. Freund<sup>17</sup>, N. Frodyma<sup>2</sup>, A. Gangapshev<sup>6,10</sup>, A. Garfagnini<sup>15,16</sup>, C. Gotti<sup>8,d</sup>, P. Grabmayr<sup>17</sup>, V. Gurentsov<sup>10</sup>, K. Gusev<sup>4,12,14</sup>, K. K. Guthikonda<sup>18</sup>, W. Hampel<sup>6</sup>, A. Hegai<sup>17</sup>, M. Heisel<sup>6</sup>, S. Hemmer<sup>15,16</sup>, G. Heusser<sup>6</sup>, W. Hofmann<sup>6</sup>, M. Hult<sup>5</sup>, L. V. Inzhechik<sup>10,e</sup>, L. Ioannucci<sup>1</sup>, J. Janicskó Csáthy<sup>14</sup>, J. Jochum<sup>17</sup>, M. Junker<sup>1</sup>, T. Kihm<sup>6</sup>, I. V. Kirpichnikov<sup>11</sup>, A. Kirsch<sup>6</sup>, A. Klimenko<sup>4,6,f</sup>, K. T. Knöpfle<sup>6</sup>, O. Kochetov<sup>4</sup>, V. N. Kornoukhov<sup>10,11</sup>, V. V. Kuzminov<sup>10</sup>, M. Laubenstein<sup>1</sup>, A. Lazzaro<sup>14</sup>, V. I. Lebedev<sup>12</sup>, B. Lehnert<sup>3</sup>, H. Y. Liao<sup>13</sup>, M. Lindner<sup>6</sup>, I. Lippi<sup>16</sup>, X. Liu<sup>13,g</sup>, A. Lubashevskiy<sup>6</sup>, B. Lubsandorzhev<sup>10</sup>, G. Lutter<sup>5</sup>, C. Macolino<sup>1</sup>, A. A. Machado<sup>6</sup>, B. Majorovits<sup>13,a</sup>, W. Maneschg<sup>6</sup>, I. Nemchenok<sup>4</sup>, S. Nisi<sup>1</sup>, C. O'Shaughnessy<sup>13,h</sup>, D. Palioselitis<sup>13</sup>, L. Pandola<sup>1</sup>, K. Pelczar<sup>2</sup>, G. Pessina<sup>7,8</sup>, A. Pullia<sup>9</sup>, S. Riboldi<sup>9</sup>, C. Sada<sup>15,16</sup>, M. Salathe<sup>6</sup>, C. Schmitt<sup>17</sup>, J. Schreiner<sup>6</sup>, O. Schulz<sup>13</sup>, B. Schwingenheuer<sup>6</sup>, S. Schönert<sup>14</sup>, E. Shevchik<sup>4</sup>, M. Shirchenko<sup>4,12</sup>, H. Simgen<sup>6</sup>, A. Smolnikov<sup>6</sup>, L. Stanco<sup>16</sup>, H. Strecker<sup>6</sup>, M. Tarka<sup>18</sup>, C. A. Ur<sup>16</sup>, A. A. Vasenko<sup>11</sup>, O. Volynets<sup>13</sup>, K. von Sturm<sup>15,16,17</sup>, V. Wagner<sup>6</sup>, M. Walter<sup>18</sup>, A. Wegmann<sup>6</sup>, T. Wester<sup>3</sup>, M. Wojcik<sup>2</sup>, E. Yanovich<sup>10</sup>, P. Zavarise<sup>1,i</sup>, I. Zhitnikov<sup>4</sup>, S. V. Zhukov<sup>12</sup>, D. Zinatulina<sup>4</sup>, K. Zuber<sup>3</sup>, G. Zuzel<sup>2</sup>

<sup>1</sup> INFN Laboratori Nazionali del Gran Sasso, LNGS, Assergi, Italy

<sup>2</sup> Institute of Physics, Jagiellonian University, Cracow, Poland

<sup>3</sup> Institut für Kern- und Teilchenphysik, Technische Universität Dresden, Dresden, Germany

<sup>4</sup> Joint Institute for Nuclear Research, Dubna, Russia

<sup>5</sup> Institute for Reference Materials and Measurements, Geel, Belgium

<sup>6</sup> Max Planck Institut für Kernphysik, Heidelberg, Germany

<sup>7</sup> Dipartimento di Fisica, Università Milano Bicocca, Milan, Italy

<sup>8</sup> INFN Milano Bicocca, Milan, Italy

<sup>9</sup> Dipartimento di Fisica, Università degli Studi di Milano e INFN Milano, Milan, Italy

<sup>10</sup> Institute for Nuclear Research of the Russian Academy of Sciences, Moscow, Russia

<sup>11</sup> Institute for Theoretical and Experimental Physics, Moscow, Russia

<sup>12</sup> National Research Centre "Kurchatov Institute", Moscow, Russia

<sup>13</sup> Max-Planck-Institut für Physik, München, Germany

<sup>14</sup> Physik Department and Excellence Cluster Universe, Technische Universität München, München, Germany

<sup>15</sup> Dipartimento di Fisica e Astronomia dell'Università di Padova, Padua, Italy

<sup>16</sup> INFN Padova, Padua, Italy

<sup>17</sup> Physikalisches Institut, Eberhard Karls Universität Tübingen, Tübingen, Germany

<sup>18</sup> Physik Institut der Universität Zürich, Zurich, Switzerland

Received: 21 June 2013 / Accepted: 2 December 2013 / Published online: 4 April 2014

© The Author(s) 2014. This article is published with open access at Springerlink.com

<sup>a</sup> e-mail: bela.majorovits@mpp.mpg.de

<sup>b</sup> Present address: CEGEP St-Hyacinthe, Quebec, Canada

<sup>c</sup> Present address: INFN LNGS, Assergi, Italy

<sup>d</sup> Also at Università di Firenze, Italy

<sup>e</sup> Also at Moscow Institute of Physics and Technology, Russia

<sup>f</sup> Also at International University for Nature, Society and Man "Dubna"

<sup>g</sup> Present address: Shanghai Jiaotong University, Shanghai, China

<sup>h</sup> Present address: University North Carolina, Chapel Hill, USA

<sup>i</sup> Present address: Dipartimento di Fisica, University of L'Aquila, L'Aquila, Italy

**Abstract** The GERmanium Detector Array (GERDA) experiment at the Gran Sasso underground laboratory (LNGS) of INFN is searching for neutrinoless double beta ( $0\nu\beta\beta$ ) decay of  $^{76}\text{Ge}$ . The signature of the signal is a monoenergetic peak at 2039 keV, the  $Q_{\beta\beta}$  value of the decay. To avoid bias in the signal search, the present analysis does not consider all those events, that fall in a 40 keV wide region centered around  $Q_{\beta\beta}$ . The main parameters needed for the  $0\nu\beta\beta$  analysis are described. A background model was devel-

oped to describe the observed energy spectrum. The model contains several contributions, that are expected on the basis of material screening or that are established by the observation of characteristic structures in the energy spectrum. The model predicts a flat energy spectrum for the blinding window around  $Q_{\beta\beta}$  with a background index ranging from  $17.6$  to  $23.8 \times 10^{-3}$  cts/(keV kg yr). A part of the data not considered before has been used to test if the predictions of the background model are consistent. The observed number of events in this energy region is consistent with the background model. The background at  $Q_{\beta\beta}$  is dominated by close sources, mainly due to  $^{42}\text{K}$ ,  $^{214}\text{Bi}$ ,  $^{228}\text{Th}$ ,  $^{60}\text{Co}$  and  $\alpha$  emitting isotopes from the  $^{226}\text{Ra}$  decay chain. The individual fractions depend on the assumed locations of the contaminants. It is shown, that after removal of the known  $\gamma$  peaks, the energy spectrum can be fitted in an energy range of 200 keV around  $Q_{\beta\beta}$  with a constant background. This gives a background index consistent with the full model and uncertainties of the same size.

## 1 Introduction

Some even–even nuclei are energetically forbidden to decay via single  $\beta$  emission, while the decay via emission of two electrons and two neutrinos is energetically allowed. The experimentally observed neutrino accompanied double beta ( $2\nu\beta\beta$ ) decay is a second order weak process with half lives of the order of  $10^{18-24}$  yr [1]. The decay process without neutrino emission, neutrinoless double beta ( $0\nu\beta\beta$ ) decay, is of fundamental relevance as its observation would imply lepton number violation indicating physics beyond the standard model of particle physics. The GERDA experiment [2] is designed to search for  $0\nu\beta\beta$  decay in the isotope  $^{76}\text{Ge}$ . This process is identified by a monoenergetic line in the energy sum spectrum of the two electrons at 2039 keV [3], the  $Q_{\beta\beta}$ -value of the decay. The two precursor experiments, the Heidelberg Moscow (HDM) and the International Germanium EXperiment (IGEX), have set limits on the half live  $T_{1/2}^{0\nu}$  of  $0\nu\beta\beta$  decay  $T_{1/2}^{0\nu} > 1.9 \times 10^{25}$  yr [4] and  $T_{1/2}^{0\nu} > 1.6 \times 10^{25}$  yr [5] (90 % C.L.), respectively. A subgroup of the HDM experiment claims to have observed  $0\nu\beta\beta$  decay with a central value of the half life of  $T_{1/2}^{0\nu} = 1.19 \times 10^{25}$  yr [6]. This result was later refined using pulse shape discrimination (PSD) [7] yielding a half life of  $T_{1/2}^{0\nu} = 2.23 \times 10^{25}$  yr. Several inconsistencies in the latter analysis have been pointed out in Ref. [8].

The design of the GERDA apparatus for the search of  $0\nu\beta\beta$  decay follows the suggestion to operate high purity germanium (HPGe) detectors directly in a cryogenic liquid that serves as cooling medium and simultaneously as ultra-pure shielding against external radiation [9]. GERDA aims in its

Phase I to test the HDM claim of a signal and, in case of no confirmation, improve this limit by an order of magnitude in Phase II of the experiment.

Prerequisites for rare-event studies are (i) extremely low backgrounds, usually expressed in terms of a background index (BI) measured in cts/(keV kg yr), and (ii) large masses and long measuring times, expressed as exposure  $\mathcal{E}$ . Reducing the background and establishing a radio-pure environment is an experimental challenge. Proper analysis methods must be applied to guarantee an unbiased analysis. The GERDA collaboration has blinded a region of  $Q_{\beta\beta} \pm 20$  keV during the data taking period [2]. During this time, analysis methods and background models have been developed and tested. The latter is described in this paper together with other parameters demonstrating the data quality.

The raw data are converted into energy spectra. If the energies of individual events fall within a range  $Q_{\beta\beta} \pm 20$  keV, these events are stored during the blinding mode in the backup files only. They are not converted to the data file that is available for analysis. This blinding window is schematically represented in Fig. 1 by the yellow area, including the red range. After fixing the calibration parameters and the background model, the blinding window was partially opened except the peak range at  $Q_{\beta\beta}$ , indicated in red in Fig. 1. The blue range covers the energies from 100 keV to 7.5 MeV. The data from this energy range were available for analysis all the time. The observable  $\gamma$  lines can be used to identify background sources. A range between 1930 and 2190 keV was then used to determine the BI. The energy regions around significant  $\gamma$  lines are excluded in the latter, as shown schematically in Fig. 1.

Data were taken until until May 2013. These data provide the exposure  $\mathcal{E}$  for Phase I. The data used in this analysis of the background are a subset containing data taken until March 2013.

The extraction of the background model is described in detail in this paper. In the process, the necessary parameters are defined for the upcoming  $0\nu\beta\beta$  analysis. An important feature is the stable performance of the germanium detectors

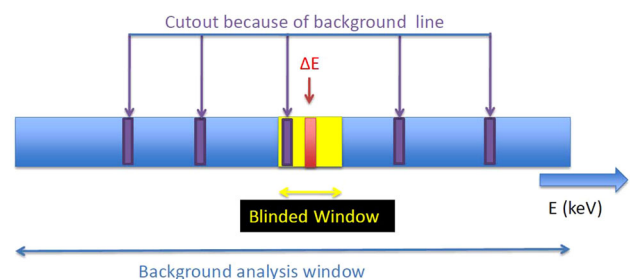


**Fig. 1** Representation of energy spectra for definition of the energy windows used in the blind analysis

enriched in  $^{76}\text{Ge}$ ; this is demonstrated for the complete data taking period (Sect. 2).

The data with exposure  $\mathcal{E}$  is used to interpolate the background within  $\Delta E$ . The expectation for the BI is given in this paper before unblinding the data in the energy range  $\Delta E$ , the region of highest physics interest.

The paper is organized as follows: after presenting the experimental details, particularly on the detectors used in Phase I of the GERDA experiment, coaxial and BEGe type (Sect. 2), the spectra and the identified background sources will be discussed (Sects. 3 and 4). These are the basic ingredients for the background decomposition for the coaxial detectors (Sect. 5) and for the BEGe detectors (Sect. 6). The models work well for both types of detectors. After cross checks of the background model (Sect. 7) the paper concludes with the prediction for the background at  $Q_{\beta\beta}$  and the prospective sensitivity of GERDA Phase I (Sect. 8).

## 2 The experiment

This section briefly recalls the main features of the GERDA experiment. The main expected background components are briefly summarized. Due to the screening of the components before installation, the known inventory of radioactive contaminations can be estimated. Finally, the stable performance of the experiment is demonstrated and the data selection cuts are discussed.

### 2.1 The hardware

The setup of the GERDA experiment is described in detail in Ref. [2]. GERDA operates high purity germanium (HPGe) detectors made from material enriched to about 86 % in  $^{76}\text{Ge}$  in liquid argon (LAr) which serves both as coolant and as shielding. A schematic view is given in Fig. 2. A stainless steel cryostat filled with  $64\text{ m}^3$  of LAr is located inside a water tank of 10 m in diameter. Only very small amounts of LAr are lost as it is cooled via a heat exchanger by liquid nitrogen. The  $590\text{ m}^3$  of high purity ( $>0.17\text{ M}\Omega\text{m}$ ) water moderate ambient neutrons and  $\gamma$  radiation. It is instrumented with 66 photo multiplier tubes (PMT) and operates as a Cherenkov muon veto to further reduce cosmic induced backgrounds to insignificant levels for the GERDA experiment. Muons traversing through the opening of the cryostat without reaching water are detected by plastic scintillator panels on top of the clean room.

Three coaxial or five BEGe detectors are mounted into each of the four strings which are lowered through a lock separating the clean room from the cryostat. The detector strings with coaxial detectors are housed in  $60\text{ }\mu\text{m}$  thin-walled copper containers permeable to LAr—called mini shroud in the following—with a distance of a few mm from the detector

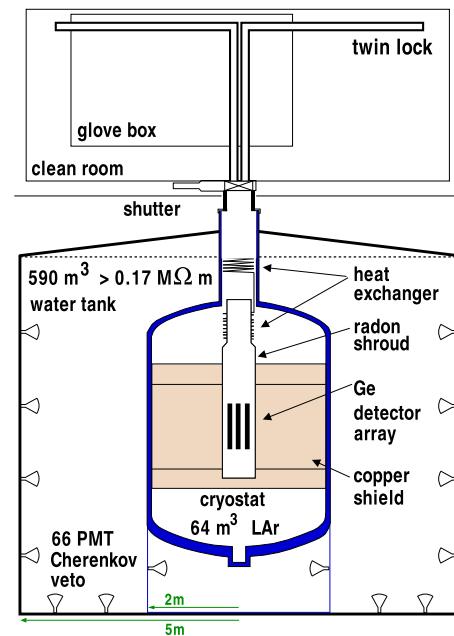


**Fig. 2** Schematic drawing of the main components of the GERDA experiment. For details see Ref. [2]

outer surfaces. A  $30\text{ }\mu\text{m}$  thin copper cylinder—called radon shroud in the following—with a diameter of 75 cm encloses the detector array. A picture of a detector string can be found in [2]. The custom made preamplifiers are operated in LAr at a distance of about 30 cm from the top of the detector array. The analog signals are digitized by 100 MHz FADCs.

All eight of the reprocessed coaxial germanium detectors from the HDM and the IGEX experiments [4,5] were deployed on 9 November 2011, together with three detectors with natural isotopic abundance. A schematic drawing of the coaxial detector type is shown in Fig. 3, top. Two enriched detectors (ANG 1 and RG 3) developed high leakage currents soon after the start of data taking and were not considered in the analysis. RG 2 was taking data for about 1 yr before it also had to be switched off due to an increase of its leakage current. In July 2012, two of the low background coaxial HPGe detectors with natural isotopic abundance, GTF 32 and GTF 45, were replaced by five enriched Broad Energy Germanium (BEGe) detectors, which follow the Phase II design of GERDA (see Fig. 3, bottom). The geometries and thus the pulse shape properties of the two types of detectors differ as discussed in Ref. [10]. One of the BEGe detectors (GD35C) showed instabilities during data taking and was not used for further analysis. The most relevant properties of all the germanium detectors are compiled in Table 1. Note, that the numbers for dead layers  $d_{dl}$  are to be interpreted as effective values, because their determination by comparison of count rates and Monte Carlo (MC) predictions depends on the precision of the model and the geometries [11].

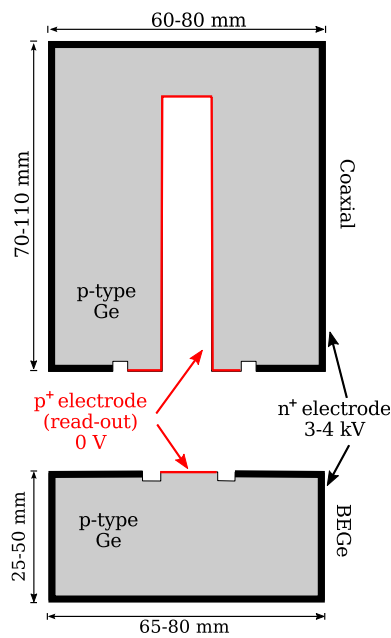


**Fig. 3** Schematic sketch of a coaxial HPGe detector (*top*) and a BEGe detector (*bottom*) with their different surfaces and dead layers (drawings not to scale)

## 2.2 Expected background sources

An important source of background is induced by cosmic radiation. Muon induced background events are efficiently vetoed by identification of Cherenkov light emitted by muons

when they pass the water tank. The number of long lived cosmogenically produced isotopes, especially  $^{68}\text{Ge}$  and  $^{60}\text{Co}$  are minimized by minimization of the time above ground during processing of the detectors and the structural materials.

Further background contributions stem from radioactivity included in the detector and structural materials or the surrounding environment, i.e. the rocks of the laboratory. The selection of materials has been described in [2]. The most important activities are discussed in the next section.

Background from  $^{42}\text{Ar}$  present in LAr was found during GERDA commissioning to be more significant than anticipated. The  $\beta$  decay of its progeny  $^{42}\text{K}$  can contribute to the background at  $Q_{\beta\beta}$  if the decay happens near detector surfaces. For GERDA Phase I coaxial detectors this background was significantly reduced by implementation of the mini shrouds. However, for the BEGe detectors this remains an important background due to their thinner surface  $n^+$  dead layer.

Another potential source of background stems from the calibration sources that have a typical initial activity of about 10–20 kBq. When in parking position they are well shielded and contribute insignificantly. Due to an accident during commissioning the experiment, one 20 kBq  $^{228}\text{Th}$  calibration source fell to the bottom of the cryostat. The BI expected from this source is around  $10^{-3}$  cts/(keV kg yr), thus, significantly less than the Phase I BI goal. Hence, the calibration source was left inside the LAr cryostat. It will be removed during the upgrade of the experiment to its second phase.

**Table 1** Main parameters for the HPGe detectors employed in the GERDA experiment: isotopic abundance of the isotope  $^{76}\text{Ge}$ ,  $f_{76}$ , total mass  $M$ , active mass  $M_{act}$ , active volume fraction  $f_{av}$  and the thickness of the effective  $n^+$  dead layer,  $d_{dl}$

Detector	$f_{76}$	$M$ (g)	$M_{act}(\Delta M_{act})$ (g)	$f_{av}(\Delta f_{av})$	$d_{dl}$ (mm)
<i>Enriched coaxial detectors</i>					
ANG 1 <sup>a</sup>	0.859 (29)	958	795 (50)	0.830 (52)	1.8 (5)
ANG 2	0.866 (25)	2833	2468 (145)	0.871 (51)	2.3 (7)
ANG 3	0.883 (26)	2391	2070 (136)	0.866 (57)	1.9 (7)
ANG 4	0.863 (13)	2372	2136 (135)	0.901 (57)	1.4 (7)
ANG 5	0.856 (13)	2746	2281 (132)	0.831 (48)	2.6 (6)
RG 1	0.855 (15)	2110	1908 (125)	0.904 (59)	1.5 (7)
RG 2	0.855 (15)	2166	1800 (115)	0.831 (53)	2.3 (7)
RG 3 <sup>a</sup>	0.855 (15)	2087	1868 (113)	0.895 (54)	1.4 (7)
<i>Enriched BEGe detectors</i>					
GD32B	0.877 (13)	717	638 (19)	0.890 (27)	1.0 (2)
GD32C	0.877 (13)	743	677 (22)	0.911 (30)	0.8 (3)
GD32D	0.877 (13)	723	667 (19)	0.923 (26)	0.7 (2)
GD35B	0.877 (13)	812	742 (24)	0.914 (29)	0.8 (3)
GD35C <sup>a</sup>	0.877 (13)	635	575 (20)	0.906 (32)	0.8 (3)
<i>Natural coaxial detectors</i>					
GTF 32 <sup>a</sup>	0.078 (1)	2321	2251 (116)	0.97 (5)	0.4 (8)
GTF 45 <sup>a</sup>	0.078 (1)	2312			
GTF 112	0.078 (1)	2965			

<sup>a</sup> Not used in this analysis

**Table 2** Gamma ray screening and  $^{222}\text{Rn}$  emanation measurement results for hardware components and BIs derived from MC simulations. The activity of the mini shroud was derived from ICP-MS measurement assuming secular equilibrium of the  $^{238}\text{U}$  decay chain. Estimates of the BI at  $Q_{\beta\beta}$  are based on efficiencies obtained by MC simulations [13, 14] of the GERDA setup

Component	Units	$^{40}\text{K}$	$^{214}\text{Bi}$ and $^{226}\text{Ra}$	$^{228}\text{Th}$	$^{60}\text{Co}$	$^{222}\text{Rn}$	BI [ $10^{-3}$ cts/(keV kg yr)]
<i>Close sources: up to 2 cm from detectors</i>							
Copper det. support	$\mu\text{Bq/det.}$	<7	<1.3	<1.5			<0.2
PTFE det. support	$\mu\text{Bq/det.}$	6.0 (11)	0.25 (9)	0.31 (14)			0.1
PTFE in array	$\mu\text{Bq/det.}$	6.5 (16)	0.9 (2)				0.1
Mini shroud	$\mu\text{Bq/det.}$		22 (7)				2.8
Li salt	mBq/kg		17 (5)				$\approx 0.003^a$
<i>Medium distance sources: 2–30 cm from detectors</i>							
CC2 preamps	$\mu\text{Bq/det.}$	600 (100)	95 (9)	50 (8)			0.8
Cables and suspension	mBq/m	1.40 (25)	0.4 (2)	0.9 (2)	76 (16)		0.2
<i>Distant sources: further than 30 cm from detectors</i>							
Cryostat	mBq					54.7 (35)	<0.7
Copper of cryostat	mBq	<784	264 (80)	216 (80)	288 (72)		] <0.05
Steel of cryostat	kBq	<72	<30	<30	475		
Lock system	mBq					2.4 (3)	<0.03
$^{228}\text{Th}$ calib. source	kBq			20			<1.0

<sup>a</sup> Value derived for 1 mg of Li salt absorbed into the surface of each detector

A significant fraction of the background is induced by contaminations of bulk materials and surfaces with nuclei from the  $^{238}\text{U}$  and  $^{232}\text{Th}$  decay chains. The  $^{238}\text{U}$  decay chain can be subdivided into three sub decay chains:  $^{238}\text{U}$  to  $^{226}\text{Ra}$ ,  $^{226}\text{Ra}$  to  $^{210}\text{Pb}$  and  $^{210}\text{Pb}$  to  $^{206}\text{Pb}$ , due to isotopes with half lives significantly longer than the live time of the experiment. Only the two latter sub decay chains are relevant in the following. The noble gas  $^{222}\text{Rn}$  ( $T_{1/2} = 3.8$  days) plays a special role, as it can further break the  $^{226}\text{Ra}$  to  $^{210}\text{Pb}$  chain due to its volatility. Whenever activities of  $^{214}\text{Bi}$  are quoted it is assumed that the chain is in secular equilibrium between  $^{226}\text{Ra}$  and  $^{210}\text{Pb}$  inside metallic materials, while for non metallic materials the equilibrium can be broken at  $^{222}\text{Rn}$ .

### 2.3 Known inventory from screening

The hardware components close to the detectors and the components of the suspension system have been tested for their radio-purity prior to installation [2]. The hardware parts at close (up to 2 cm) and medium (up to 30 cm) distance from the detectors have been screened using HPGe screening facilities or ICP-MS measurements, while the parts in the lock system have been tested for  $^{222}\text{Rn}$  emanation [12]. Some materials proved to have low, but measurable, radioactive contaminations. Table 2 quotes the total measured activities and limits of the most significant screened components and their expected contribution to the BI close to  $Q_{\beta\beta}$ . As the  $^{222}\text{Rn}$  emanation rate in the cryostat with its copper lining and the lock system is on the order of 60 mBq, some  $^{214}\text{Bi}$  may be expected in the LAr surrounding of the detectors. Assuming a homoge-

neous distribution of  $^{222}\text{Rn}$  in the LAr, this would result in a contribution to the BI at  $Q_{\beta\beta}$  of  $7 \times 10^{-4}$  cts/(keV kg yr). To reduce this latter contribution to the GERDA background, the radon shroud was installed around the array with the intention to keep  $^{222}\text{Rn}$  transported by LAr convection at sufficient distance from the detectors.

Additionally, Li salt that is used to dope  $n^+$  surfaces of the detectors was screened. It is not precisely known how much Li diffuses into the crystal. A rough estimation assuming an  $n^+$  Li doping of  $10^{16}$  Li nuclei per  $\text{cm}^3$  germanium results in an overall Li weight per detector of  $\approx 5 \mu\text{g}$  which leads to negligible background contributions even if it is assumed that the  $^{226}\text{Ra}$  contamination diffuses into the germanium with the same efficiency as Li.

The measured activities in the hardware components within 2 cm from the detectors lead to a total contribution to the BI of  $\approx 3 \times 10^{-3}$  cts/(keV kg yr) using efficiencies obtained by MC simulations [13, 14]. From the medium distance contributions  $\approx 10^{-3}$  cts/(keV kg yr) are expected, while the far sources contribute with  $< 10^{-3}$  cts/(keV kg yr). As detailed in Ref. [2] the extrapolated background rates for all contaminations were predicted to be tolerable for Phase I and to yield a BI of  $< 10^{-2}$  cts/(keV kg yr).

### 2.4 Run parameters and efficiencies

The muon veto system started operation in December 2010 and ran up to 21 May 2013, when the data taking for the  $0\nu\beta\beta$  analysis was stopped. Its stable performance is shown in the top graph of Fig. 4. The interruptions were due to the test and

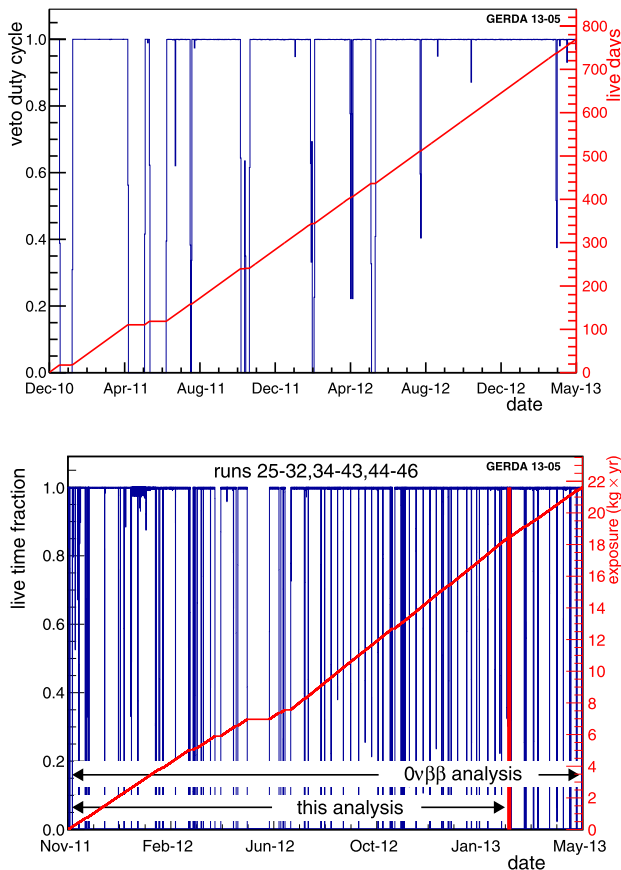


**Fig. 4** Live time fraction of the data acquisition for the muon veto (*top*) and for the HPGe detectors (*bottom*). The spikes in the live time fraction arise from the regular calibration measurements. The development of the exposure  $\mathcal{E}$  of the enriched detectors (*bottom*) and the total live time of the muon veto system (*top*) is also shown. The *red vertical line* indicates the end of the data range for the evaluation of the background model

installation of the plastic panel in April/May 2011 and due to short calibrations. The probability that a muon induced event in the detectors is accompanied by a signal in the veto (overall muon rejection efficiency) is  $\varepsilon_{\mu\nu} = 0.991^{+0.003}_{-0.004}$ , reducing the contribution of the muons to the BI to  $<10^{-3}$  cts/(keV kg yr) [15]. No evidence for delayed coincidences between  $\mu$  veto events and germanium events was found.

The bottom graph in Fig. 4 demonstrates the live time fraction of data taking. The interruption in May 2012 was due to temperature instabilities in the GERDA clean room, while the interruption in July 2012 was due to the insertion of five Phase II type BEGe detectors. The analysis presented here considers data taken until 3 March 2013, corresponding to a live time of 417.19 days and an exposure of  $\mathcal{E} = 16.70$  kg yr for the coaxial detectors; the four BEGe detectors acquired between 205 and 230 days of live time each, yielding a total exposure of  $\mathcal{E} = 1.80$  kg yr. The end of run 43 in March is marked by the red vertical line in Fig. 4, bottom.

The data have been processed using algorithms and data selection procedures [16, 17] implemented in the GERDA soft-

ware framework [18]. A set of quality cuts, described in detail in Ref. [16], is applied to identify and reject unphysical events, e.g. generated by discharges or by electromagnetic noise. The cuts take into account several parameters of the charge pulse, such as rise time, baseline fluctuations and reconstructed position of the leading edge. The cuts also identify events having a non-flat baseline, e.g. due to a previous pulse happening within a few hundreds of  $\mu$ s. Moreover, events in which two distinct pulses are observed during the digitization time window (80  $\mu$ s) are marked as pile-up and are discarded from the analysis. From the total number of triggers roughly 91 % are kept as physical events. Due to the very low counting rate, the GERDA data set has a negligible contamination of accidental pile-up events and the selection efficiency for genuine  $0\nu\beta\beta$  events is hence practically unaffected by the anti pile-up cuts. Similarly, the loss of physical events above 1 MeV due to mis-classification by the quality cuts is less than 0.1 %.

The linearity and the long term stability of the energy scale as well as the energy resolution given as full width at half maximum (FWHM) were checked regularly with  $^{228}\text{Th}$  sources. Between calibrations the stability of the gain of the preamplifiers was monitored by test pulses induced on the test inputs of the preamplifiers. Whenever unusual fluctuations on the preamplifier response were observed, calibrations were performed. The linearity of the preamplifier has been checked using test pulses up to an energy range of 6 MeV. It was found that between 3 and 6 MeV the calibration has a precision of better than 10 keV; above 6 MeV some channels exhibit larger non-linearity.

Physical events passing the quality cuts are excluded from the analysis if they come in coincidence within 8  $\mu$ s with a valid muon veto signal (muon veto cut) or if they have energy deposited in more than one HPGe detector (anti-coincidence cut). The anti-coincidence cut does not further affect the selection efficiency for  $0\nu\beta\beta$  decays, since only events with full energy deposit of 2039 keV are considered. The dead time induced by the muon veto cut is practically zero as the rate of  $(9.3 \pm 0.4) \times 10^{-5}$ /s of events coincident between germanium detectors and the GERDA muon veto system is very low.

The stability of the energy scale was checked by the time dependence of the peak position for the full energy peak at 2614.5 keV from the  $^{228}\text{Th}$  calibration source. The maximal shifts are about 2 keV with the exception of 5 keV for the GD32B detector. The distributions of the shifts are fitted by a Gaussian with FWHM amounting to 1.49 keV for the coaxial and to 1.01 keV for the BEGe detectors. The respective uncertainties are smaller than 10 %. The shifts are tolerable compared to the energy resolution.

To obtain the energy resolution at  $Q_{\beta\beta}$  the results from the calibration measurements are interpolated to the energy  $Q_{\beta\beta}$

**Table 3** Energy resolutions (FWHM) in keV of the enriched detectors at  $Q_{\beta\beta}$ . For definition of the data sets see Sect. 3.2

SUM-coax		SUM-bege	
Detector	FWHM [keV]	Detector	FWHM [keV]
ANG 2	5.8 (3)	GD32B	2.6 (1)
ANG 3	4.5 (1)	GD32C	2.6 (1)
ANG 4	4.9 (3)	GD32D	3.7 (5)
ANG 5	4.2 (1)	GD35B	4.0 (1)
RG 1	4.5 (3)		
RG 2	4.9 (3)		
Mean coax	4.8 (2)	Mean BEGe	3.2 (2)

using the standard expression  $FWHM = \sqrt{a^2 + b^2 \cdot E}$  [19]. The energy resolution during normal data taking is slightly inferior to the resolution during calibration measurements. The resulting offset was determined by taking the difference between the resolution of the  $^{42}\text{K}$  line and the interpolated resolution determined from calibrations. The scaled offset is added to the resolution at  $Q_{\beta\beta}$  expected from calibration measurements. The FWHM of all enriched detectors at 2614.5 keV is determined to be between 4.2 and 5.8 keV for the coaxial detectors and between 2.6 and 4.0 keV for the BEGes. The resolutions are stable in time to within 0.3 keV for the BEGes and to within 0.2 keV for the coaxial detectors. The resolutions of all relevant enriched detectors are shown in Table 3.

The total exposure  $\mathcal{E}$  used for the upcoming  $0\nu\beta\beta$  analysis is given by the sum of products of live time  $t_i$  and total mass  $M_i$ , where the index  $i$  runs over the active detectors. For the evaluation of  $T_{1/2}^{0\nu}$ , the acceptance of PSD cuts,  $\varepsilon_{psd}$ , the efficiencies  $\varepsilon_{res}$  to find the  $0\nu\beta\beta$  within the analysis window  $\Delta E$  and the detection efficiency of the  $0\nu\beta\beta$  decay  $\varepsilon_{fep}$  are needed. The energy of  $0\nu\beta\beta$  events is assumed to be Gaussian distributed with a mean equal to the  $Q_{\beta\beta}$  value. An exposure averaged efficiency is defined as

$$\langle \varepsilon \rangle = \frac{\sum_i f_{av,i} f_{76,i} M_i t_i \varepsilon_{fep,i}}{\mathcal{E}}, \tag{1}$$

where  $f_{av,i}$  is the active volume fraction and  $f_{76,i}$  the enrichment fraction of the individual detector  $i$ .

With  $N_A$ , the Avogadro number,  $m_{enr}$  the molar mass of the germanium and  $N$  the number of observed counts the half life reads

$$T_{1/2}^{0\nu} = \frac{\ln 2 \cdot N_A}{m_{enr}} \frac{\mathcal{E}}{N} \langle \varepsilon \rangle \varepsilon_{psd} \varepsilon_{res}. \tag{2}$$

### 3 Background spectra and data sets

The main objective of  $0\nu\beta\beta$  experiments is the possible presence of a peak at  $Q_{\beta\beta}$ . All other parts of the energy spectrum can be considered as background. As detectors have their own history and experienced different surroundings their energy spectra might vary. Furthermore, the experimental conditions might change due to changes of the experimental setup. Thus, a proper selection and grouping of the data can optimize the result. This selection is performed on the ‘‘background data’’ and will be applied in the same way to the ‘‘ $0\nu\beta\beta$  data’’.

#### 3.1 Background spectra

Figure 5 compares the energy spectra in the range from 100 keV to 7.5 MeV obtained from the three detector types: (i) the enriched coaxial detectors (top), (ii) the enriched BEGe detectors (middle) and (iii) the coaxial low background detector GTF 112 (bottom) with natural isotopic abundance.

Some prominent features can be identified. The low energy part up to 565 keV is dominated by  $\beta$  decay of cosmogenic  $^{39}\text{Ar}$  in all spectra. Slight differences in the spectral shape between the coaxial and BEGe type detectors result from differences in detector geometry and of the  $n^+$  dead layer thickness. Between 600 and 1500 keV the spectra of the enriched detectors exhibit an enhanced continuous spectrum due to  $2\nu\beta\beta$  decay [20]. In all spectra,  $\gamma$  lines from the decays of  $^{40}\text{K}$  and  $^{42}\text{K}$  can be identified, the spectra of the enriched coaxial detectors contain also lines from  $^{60}\text{Co}$ ,  $^{208}\text{Tl}$ ,  $^{214}\text{Bi}$ ,  $^{214}\text{Pb}$  and  $^{228}\text{Ac}$ . A peak-like structure appears around 5.3 MeV in the spectrum of the enriched coaxial detectors. This can be attributed to the decay of  $^{210}\text{Po}$  on the detector  $p^+$  surfaces. Further peak like structures at energies of 4.7, 5.4 and 5.9 MeV can be attributed to the  $\alpha$  decays on the detector  $p^+$  surface of  $^{226}\text{Ra}$ ,  $^{222}\text{Rn}$  and  $^{218}\text{Po}$ , respectively. These events are discussed in more detail below. There are no hints for contamination of the detector  $p^+$  surfaces with isotopes from the  $^{232}\text{Th}$  decay chain in the data analyzed here.

The observed background rate of the coaxial enriched detectors in the energy region between 1550 and 3000 keV in 15 calendar day intervals is displayed in Fig. 6. The data are corrected for live time. Apart from the time period directly after the deployment of the BEGe detectors to the GERDA cryostat in July 2012, the rate in this energy region was stable within uncertainties over the whole time period.

#### 3.2 Data sets

For further analysis of the background contributions the data are divided into different subsets based on the observed BI near  $Q_{\beta\beta}$ . In the energy region between 600 and 1500 keV, the spectrum of the enriched detectors is dominated by  $2\nu\beta\beta$

**Fig. 5** Spectra taken with all the enriched coaxial (top) and BEGe (middle) and a non-enriched (bottom) detector. The blinding window of  $Q_{\beta\beta} \pm 20$  keV is indicated as green line. The bars in the color of the histogram represent the 200 keV region from which the BI of the dataset is determined

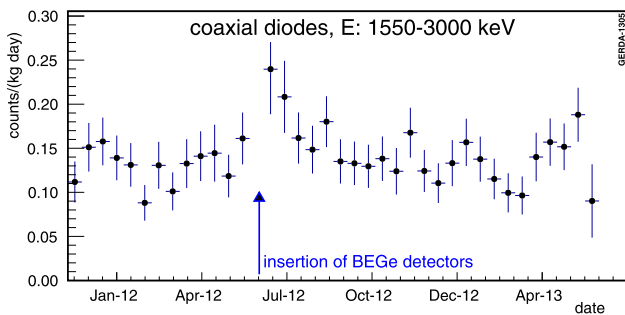
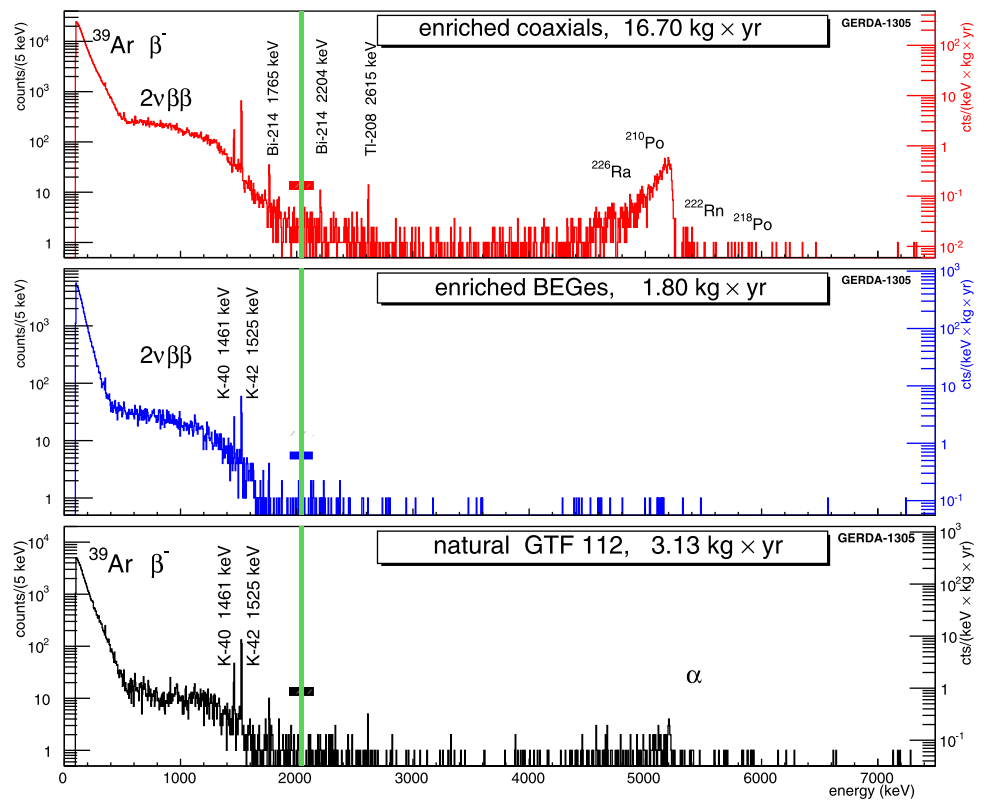


**Fig. 6** Time distribution of background rate of the enriched coaxial detectors in the energy range between 1550 and 3000 keV in 15 day intervals. An increase of the BI after BEGe deployment in July 2012 is clearly visible

**Table 4** Data sets, the detectors considered therein and their exposures  $\mathcal{E}$  for the data used for this analysis and the upcoming  $0\nu\beta\beta$  analysis.  $\mathcal{E}$  is calculated from the total detector mass

Data set	Detectors	Exposure $\mathcal{E}$	
		This analysis (kg yr)	$0\nu\beta\beta$ analysis (kg yr)
<i>SUM-coax</i>	All enriched coaxial	16.70	19.20
<i>GOLD-coax</i>	All enriched coaxial	15.40	17.90
<i>SILVER-coax</i>	All enriched coaxial	1.30	1.30
<i>GOLD-nat</i>	GTF 112	3.13	3.98
<i>GOLD-hdm</i>	ANG 2, ANG 3, ANG 4, ANG 5	10.90	12.98
<i>GOLD-igex</i>	RG 1, RG 2	4.50	4.93
<i>SUM-bege</i>	GD32B, GD32C, GD32D, GD35B	1.80	2.40

decays. Thus, characteristic  $\gamma$  lines expected from known background contributions might be visible only with the natural GTF 112 detector.

Data taken with enriched coaxial detectors in runs that were not affected by the experimental performance such as drift in gain stability, deterioration of energy resolution etc. are contained in the *SUM-coax* data set. The energy spectrum of this data set is shown in Fig. 5, top. It has an overall exposure of 16.70 kg yr (see also Table 4). The higher BI observed after the deployment of the BEGe detectors dropped to the previous level after approximately 30 days as shown in Fig. 6. Hence, the coaxial data are split: the

*SILVER-coax* data set contains data taken during the 30 days after the BEGe detector deployment. The *GOLD-coax* data set contains the rest of the data. The detectors from the HDM and IGEX experiments have different production, processing and cosmic ray exposure history. A different background composition could be expected, despite their common surface reprocessing before insertion into the GERDA experiment. Indeed,  $^{210}\text{Po}$   $\alpha$ -contaminations are most prominent on detectors from the HDM experiment (see Table 6). The *GOLD-coax* data set is therefore divided into two subsets



*GOLD-hdm* and *GOLD-igex* to verify the background model on the two subsets individually. The *SUM-bege* data set contains the data taken with four out of the five Phase II BEGe detectors. The *GOLD-nat* data set contains data taken with the low-background detector GTF 112 of natural isotopic composition.

The data sets used in this analysis, the detectors selected and the exposures  $\mathcal{E}$  of the data used in this analysis and separately for the upcoming  $0\nu\beta\beta$  analysis are listed in Table 4.

#### 4 Background sources and their simulation

The largest fraction of the GERDA Phase I exposure was taken with the coaxial detectors from the HDM and IGEX experiments. Thus, the background model was developed for these detectors first. Some preliminary results were presented in Ref. [21].

Background components that were identified in the energy spectra (see Sect. 3.1) or that were known to be present in the vicinity of the detectors (see Table 2) were simulated using the MAGE code [22] based on GEANT4 [23, 24]. The expected BIs due to the neutron and muon fluxes at the LNGS underground laboratory have been estimated to be of the order  $10^{-5}$  cts/(keV kg yr) [25] and  $10^{-4}$  cts/(keV kg yr) [15] in earlier works. These contributions were not considered in this analysis. Also other potential background sources for which no direct evidence could be found were not taken into consideration.

It should be mentioned that some isotopes can cause peaks at or close to the  $Q_{\beta\beta}$  value of  $^{76}\text{Ge}$ . All known decays that lead to  $\gamma$  emission with  $\sim 2040$  keV either have very short half lives or have significant other structures (peaks) that are not observed in the GERDA spectra. Three candidates are  $^{76}\text{Ge}$  [25], which can undergo neutron capture,  $^{206}\text{Pb}$  [26], which has a transition that can be excited by inelastic neutron scattering and  $^{56}\text{Co}$  that decays with a half life of 77 days. None of the strong prompt  $\gamma$  lines at 470, 861, 4008 and 4192 keV from neutron capture on  $^{76}\text{Ge}$  could be identified. In case of inelastic neutron scattering off  $^{206}\text{Pb}$ , peaks would be expected to appear at 898, 1705 and 3062 keV. These are not observed. In case of a  $^{56}\text{Co}$  contamination peaks would be expected at 1771, 2598 and 3253 keV, none of which is observed. Hence, these sources are not considered in the following for the simulation of the background components.

The GERDA Phase I detectors and the arrangement of the germanium detector array with four detector strings ('array' in Table 5) were implemented into the MAGE code. Simulations of contaminations of the following hardware components were performed (see Figs. 2, 3 and Ref. [2]): inside the germanium, on the  $p^+$  and  $n^+$  surfaces of the detectors, in the liquid argon close to the  $p^+$  surface, homogeneously distributed in the LAr, in the detector assembly represent-

ing contaminations in or on the detector holders and their components, the mini shroud, the radon shroud and the heat exchanger. Note, that the thicknesses of the detector assembly components, the shrouds and the heat exchanger are significantly smaller than the mean free path of the relevant simulated  $\gamma$  particles in the given material, thus, no significant difference can be expected between the resulting spectra of bulk and surface contaminations. Various (DL) thicknesses were considered. The  $n^+$  dead layer thicknesses  $d_{dl}(n^+)$  of the detectors were implemented according to the values reported in Table 1. Spectra resulting from contaminations on effective  $p^+$  dead layer thicknesses  $d_{dl}(p^+)$  of 300, 400, 500 and 600 nm were simulated.

Most of the identified sources for contaminations were simulated. However,  $\gamma$  induced energy spectra from sources with similar distances to the detectors have similar shapes that can not be disentangled with the available exposure. Representatively for  $\gamma$  contaminations in the close vicinity of the detectors (up to 2 cm from a detector) events in the detector assembly were simulated. Spectra due to contaminations at medium distances (between 2 and 30 cm), such as the front end electronics or the cable suspension system are represented by simulations of events in the radon shroud, while spectra resulting from distant sources (further than 30 cm) are represented by simulation of contaminations in or on the heat exchanger (see Fig. 2). The contributions of the cryostat and water tank components to the BI have not been considered in this analysis. It has been shown in earlier work that they contribute to the GERDA BI with  $< 10^{-4}$  cts/(keV kg yr) [14].

The simulated energy spectra were smeared with a Gaussian distribution with an energy dependent FWHM width corresponding to the detector resolution. The spectra for this analysis resulting from different contaminations in different locations of the experiment are summarized in Table 5.

##### 4.1 $\alpha$ events from $^{226}\text{Ra}$ , $^{222}\text{Rn}$ and $^{210}\text{Po}$ contaminations

Strong contributions from  $^{210}\text{Po}$  can be observed in the energy spectra shown in Fig. 5. No other  $\alpha$  peaks with similar intensity can be identified. This is indication for a surface  $^{210}\text{Po}$  contamination of the detectors. However, there are also hints for other peak like structures at 4.7, 5.4 and 5.9 MeV. These can be attributed to the decays of  $^{226}\text{Ra}$ ,  $^{222}\text{Rn}$  and  $^{218}\text{Po}$  on  $p^+$  detectors surfaces, respectively. However, the decay chain is clearly broken at  $^{210}\text{Pb}$ . Screening measurements indicate the presence of  $^{226}\text{Ra}$  in the vicinity of the detectors, in or on the mini shroud and of  $^{222}\text{Rn}$  in LAr. Thus, decays from  $^{222}\text{Rn}$  and its daughters are also expected in LAr (see Table 2).

Due to the short range of  $\alpha$  particles in germanium and LAr of the order of tens of  $\mu\text{m}$ , only decays occurring on or in the close vicinity (few  $\mu\text{m}$ ) of the  $p^+$  surface (assumed

dead layer thickness roughly 300 nm) can contribute to the measured energy spectrum as the  $n^+$  dead layer thickness is roughly 1 mm. Additionally,  $\alpha$  decays occurring on the

**Table 5** Summary of simulated background components for the coaxial detectors. For the  $p^+$  dead layers  $d_{dl_{p^+}}$  the thicknesses of 100, 200, 300, ..., 1000 nm were simulated. The  $^{226}\text{Ra}$  chain comprises the isotopes  $^{226}\text{Ra}$ ,  $^{222}\text{Rn}$ ,  $^{218}\text{Po}$ , and  $^{214}\text{Po}$ ; the  $^{222}\text{Rn}$  chain comprises the isotopes  $^{222}\text{Rn}$ ,  $^{218}\text{Po}$ , and  $^{214}\text{Po}$

Source	Location	Simulation	Events simulated
$^{210}\text{Po}$	$p^+$ surface	Single det., $d_{dl_{p^+}}$	$10^9$
$^{226}\text{Ra}$ chain	$p^+$ surface	Single det., $d_{dl_{p^+}}$	$10^9$
$^{222}\text{Rn}$ chain	LAr in bore hole	Single det., $d_{dl_{p^+}}$	$10^9$
$^{214}\text{Bi}$ and $^{214}\text{Pb}$	$n^+$ surface	Single det.	$10^8$
	Mini shroud	Array	$10^9$
	Detector assembly	Array	$10^8$
	$p^+$ surface	Single det.	$10^6$
	Radon shroud	Array	$10^9$
	LAr close to $p^+$ surface	Single det.	$10^6$
$^{208}\text{Tl}$ and $^{212}\text{Bi}$	Detector assembly	Array	$10^8$
	Radon shroud	Array	$10^9$
	Heat exchanger	Array	$10^{10}$
$^{228}\text{Ac}$	Detector assembly	Array	$10^8$
	Radon shroud	Array	$10^9$
$^{42}\text{K}$	Homogeneous in LAr	Array	$10^9$
	$n^+$ surface	Single det.	$10^8$
	$p^+$ surface	Single det.	$10^6$
$^{60}\text{Co}$	Detectors	Array	$2.2 \times 10^7$
	Detector assembly	Array	$10^7$
$2\nu\beta\beta$	Detectors	Array	$2.2 \times 10^7$
$^{40}\text{K}$	Detector assembly	Array	$10^8$

groove of the detector (see Fig. 3) may deposit energy in the active volume. For this part of the surface, however, no information on the actual dead layer thickness is available. The energy deposited in the active volume of the detector by surface or close to surface  $\alpha$  particles is very sensitive to the thickness of the dead layer and on the distance of the decaying nucleus from the detector surface.

All  $\alpha$  decays in the  $^{226}\text{Ra}$  to  $^{210}\text{Pb}$  sub-decay chain and the  $^{210}\text{Po}$  decay have been simulated on the  $p^+$  detector surface separately. Additionally, the decays in the chain following the  $^{226}\text{Ra}$  decay were simulated assuming a homogeneous distribution in a volume extending up to 1 mm from the  $p^+$  surface in LAr.

The resulting spectral shapes for  $^{210}\text{Po}$  on the  $p^+$  detector surface and for  $^{222}\text{Rn}$  in liquid argon are displayed in Fig. 7. The individual decays on the  $p^+$  surface result in a peak like structure with its maximum at slightly lower energies than the corresponding  $\alpha$  decay energy with a quasi exponential tail towards lower energy. The decays occurring in LAr close to the  $p^+$  surface result in a broad spectrum without any peak like structure extending to lower energies.  $\alpha$  decays of the other isotopes result in similar spectral shapes with different maximum energies.

#### 4.2 $^{214}\text{Bi}$ and $^{214}\text{Pb}$

The screening measurements indicate that the  $^{226}\text{Ra}$  daughters  $^{214}\text{Bi}$  and  $^{214}\text{Pb}$  are present in the vicinity of the detector array. Additionally, these isotopes are also expected on the detector  $p^+$  surface and in its close surrounding resulting from the  $^{226}\text{Ra}$  contamination of the detector surfaces. The spectra expected from decays of  $^{214}\text{Bi}$  and  $^{214}\text{Pb}$  in or on the radon shroud, the mini shroud, the detector assembly, on the  $n^+$  and  $p^+$  surfaces and in LAr inside the bore hole (BH) of the detector to represent decays close to the  $p^+$  detector surfaces have been simulated.  $^{214}\text{Bi}$  and  $^{214}\text{Pb}$  are the only isotopes in the  $^{226}\text{Ra}$  to  $^{210}\text{Pb}$  chain decaying by  $\beta$  decay accompanied by emission of high energy  $\gamma$  particles. Except for contaminations of the  $p^+$  surfaces that have been described in the previous section, the mean free paths of

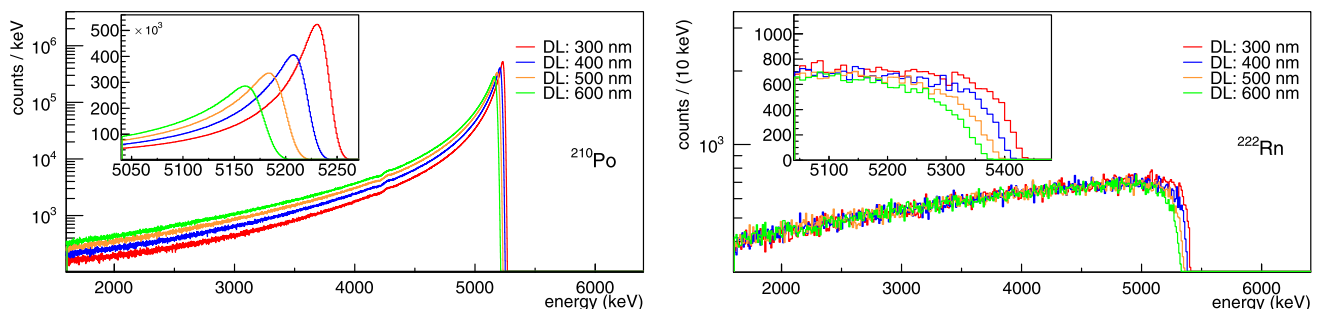


**Fig. 7** Simulated spectra resulting from  $^{210}\text{Po}$  decays on the  $p^+$  surface (left) and from  $^{222}\text{Rn}$  in LAr close to the  $p^+$  surface (right) for different dead layer (DL) thicknesses. The spectra are scaled arbitrarily for visual purposes

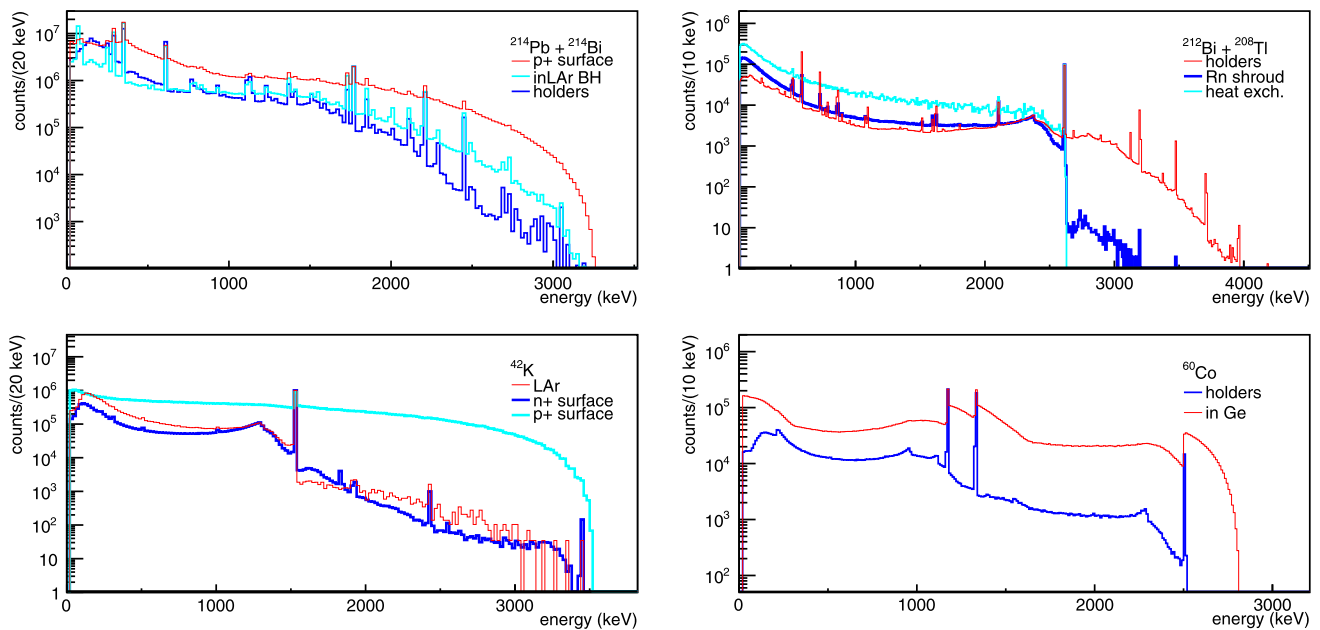


**Fig. 8** Simulated spectra for different background contributions at different source locations. Spectra are scaled arbitrarily for visual purposes.  $^{214}\text{Bi}$  and  $^{214}\text{Pb}$  on the  $p^+$  detector surface and in LAr of the bore hole close to the  $p^+$  surface (*upper left*),  $^{228}\text{Th}$  in the detector

detector assembly, the radon shroud and on the heat exchanger (*upper right*)  $^{42}\text{K}$  homogeneous in LAr, on the  $n^+$  and on the  $p^+$  surfaces (*lower left*) and  $^{60}\text{Co}$  in the detector assembly and in the germanium (*lower right*)

the  $\alpha$ -particles emitted in the decay chain are much smaller in LAr and germanium than the distance of the contamination sources from the detector active volume. Hence, only the decays of  $^{214}\text{Bi}$  and  $^{214}\text{Pb}$  can contribute to the background in the energy region of interest (RoI). These isotopes are assumed to be in equilibrium.

The spectral shapes obtained by the simulation of  $^{214}\text{Bi}$  and  $^{214}\text{Pb}$  decays in the detector assembly, on the  $p^+$  surface and inside the bore hole of the detector are shown in Fig. 8. The spectral shapes resulting from decays in or on the detector assembly components, the mini shroud and on the  $n^+$  surface turn out to be very similar. Hence, these three are treated together and are represented by the spectrum obtained for  $^{214}\text{Bi}$  and  $^{214}\text{Pb}$  decays inside the detector assembly. The spectral shape from decays in the radon shroud exhibits a much lower peak to continuum ratio at lower energies ( $E < 1500$  keV), while for higher energies the spectral shape is similar to the one obtained from simulations of decays in the detector assembly. For  $^{214}\text{Bi}$  and  $^{214}\text{Pb}$  decays on the  $p^+$  surface and, to some extent also inside the LAr of the bore hole, the peak to continuum ratio is much reduced at higher energies because of the sensitivity to the electrons due to the thin  $p^+$  dead layer.

#### 4.3 $^{228}\text{Ac}$ and $^{228}\text{Th}$

The presence of  $^{228}\text{Th}$  is expected from screening measurements in the front end electronics and the detector suspension system. The characteristic  $\gamma$  line at 2615 keV can be clearly

identified in the spectra of the enriched coaxial detectors and the detector with natural isotopic abundance shown in Fig. 5. Possible locations for  $^{228}\text{Th}$  contaminations are the detector assembly and the mini shrouds in the close vicinity, the radon shroud and the heat exchanger of the LAr cooling system at the top of the cryostat.

As only negligible hints of  $^{232}\text{Th}$  or  $^{228}\text{Th}$  surface contaminations were observed,  $\alpha$ -decays resulting from the  $^{232}\text{Th}$  decay chain are not considered in the following.

No significant top–bottom asymmetries in the count rates of the  $^{208}\text{Tl}$  and  $^{214}\text{Bi}$   $\gamma$  lines could be observed. This indicates that the front end electronics and suspension system above the detector array (medium distance sources) and the calibration source at the bottom of the cryostat (far source) are not the main background contributions.

As  $^{228}\text{Ac}$  and  $^{228}\text{Th}$  do not necessarily have to be in equilibrium, the two parts of the decay chain were simulated separately. From the sub-decay chain following the  $^{228}\text{Th}$  decay only the contributions from the  $^{212}\text{Bi}$  and  $^{208}\text{Tl}$  decays were simulated, as these are the only ones emitting high energetic  $\gamma$  rays and electrons that can reach the detectors.

The resulting spectral shapes are shown in Fig. 8. For  $^{228}\text{Th}$  contaminations in or on the radon shroud and the heat exchanger the continuum above the 2615 keV line is suppressed, while for sources in or on the detector assembly and the mini shroud the continuum above the 2615 keV peak can be significant due to summation of two  $\gamma$  rays or of an emitted electron and a  $\gamma$  particle.

The simulated spectral shapes resulting from  $^{228}\text{Ac}$  decays differ mainly for energies  $E < 1$  MeV. Generally, the peak to continuum ratio is higher for the spectrum obtained with contamination inside the detector assembly.

#### 4.4 $^{42}\text{Ar}$

While the distribution of  $^{42}\text{Ar}$  is homogeneous inside LAr, the short lived ionized decay product  $^{42}\text{K}$  ( $T_{1/2} = 12.3$  h) can have a significantly different distribution due to drifts of the  $^{42}\text{K}$  ions inside the electric fields that are present near the detectors. Spectra for three  $^{42}\text{K}$  distributions have thus been simulated: (i) homogeneous in LAr in a volume of  $6.6\text{ m}^3$  centered around the full detector array, (ii) on the  $n^+$  and (iii) on the  $p^+$  detector surface of the detectors. The  $n^+$  surface has a thickness comparable to the absorption length of the electrons emitted in the  $^{42}\text{K}$  decays in germanium. In the  $^{42}\text{K}$   $n^+$  surface simulation a 1.9 mm dead layer thickness was used, typical for the coaxial detectors. The resulting spectral shape is similar to the one obtained for  $^{42}\text{K}$  homogeneous distribution in LAr. Also, as the spectral shape is not expected to vary strongly between the detectors,  $^{42}\text{K}$  on the  $p^+$  surface was simulated only for a single detector. In this case a much higher contribution at high energies is present due to the electrons in the  $^{42}\text{K}$  decay. Consequently a much lower 1525 keV peak to continuum ratio is expected. The simulated spectral shapes are shown in Fig. 8.

#### 4.5 $^{60}\text{Co}$

Two simulated spectral shapes were used for the background decomposition, one for  $^{60}\text{Co}$  in the detector vicinity and one for  $^{60}\text{Co}$  inside the detectors. The resulting spectral shapes are shown in Fig. 8. The peak to continuum ratios are significantly different due to the electron emitted in the decay that can only deposit energy in the detector for a contamination in the close vicinity of the detector but is shielded efficiently by the liquid argon for contaminations further away.

#### 4.6 $2\nu\beta\beta$ decay

The spectral shape induced by  $2\nu\beta\beta$  decay of  $^{76}\text{Ge}$  was simulated with a homogeneous distribution of  $^{76}\text{Ge}$  inside each individual detector. Decays inside the active volume and the dead layer of the detectors were simulated separately and summed later weighted by their mass fractions. The spectral shape of the electrons emitted in  $2\nu\beta\beta$  decay as reported in Ref. [28] and implemented in the DECAY0 event generator was used.

#### 4.7 $^{40}\text{K}$

Screening measurements revealed that contaminations with  $^{40}\text{K}$  are expected in the detector assembly, the nearby front

end electronics, and in the near part of the detector suspension system. The 1460 keV  $\gamma$  line intensity is, within uncertainty, the same for the individual detectors. There is no reasonable explanation for an isotropic distant source. Hence, in the analysis it is assumed that the  $^{40}\text{K}$  contamination is in the detector assembly.

## 5 Background decomposition

A global model that describes the background spectrum was obtained by fitting the simulated spectra of different contributions to the measured energy spectrum using a Bayesian fit. A detailed description of the statistical method is given in Sect. 5.1.

First, the high energy part of the spectrum was analyzed. Above 3.5 MeV, the Q-value of  $^{42}\text{K}$ , the main contribution to the energy spectrum is expected to come from  $\alpha$  decays close to or on the thin dead layers on the detector  $p^+$  surfaces. The time distribution of the events above 3.5 MeV gives information on the origin of those events. The event rate distribution was therefore analyzed a priori to check the assumptions on the sources of  $\alpha$  induced events. The spectrum in the 3.5–7.5 MeV region was then analyzed by fitting it with the simulated spectra resulting from  $\alpha$  decays from isotopes in the  $^{226}\text{Ra}$  decay chain. The spectral model developed for the  $\alpha$  induced events also allows one to gain information on the background due to  $^{214}\text{Bi}$  in the  $^{226}\text{Ra}$  decay chain.

Subsequently, the energy range of the fit was enlarged to include as much data as possible for a higher accuracy of the model, including  $Q_{\beta\beta}$  of  $^{76}\text{Ge}$ . The background components discussed in Sect. 4 are used in the spectral analysis. A minimum fit was performed by taking only a minimum amount of well motivated close background sources into account. In a maximum fit further simulated background components, representing also medium distance and distant sources, were added to the model. The analysis was repeated for the different data sets and the obtained global models were used to derive the activities of the different contaminations.

### 5.1 Statistical analysis

The analyses of both event rate and energy distributions were carried out by fitting binned distributions. The probability of the model and its parameters, the posterior probability is given from Bayes theorem as

$$P(\lambda|\mathbf{n}) = \frac{P(\mathbf{n}|\lambda)P_0(\lambda)}{\int P(\mathbf{n}|\lambda)P_0(\lambda)d\lambda}, \quad (3)$$

where  $P(\mathbf{n}|\lambda)$  denotes the likelihood and  $P_0(\lambda)$  the prior probability of the parameters. The likelihood is written as the product of the probability of the data given the model and parameters in each bin

$$P(\mathbf{n}|\lambda) = \prod_i P(n_i|\lambda_i) = \prod_i \frac{e^{-\lambda_i} \lambda_i^{n_i}}{n_i!}, \tag{4}$$

where  $n_i$  is the observed number of events and  $\lambda_i$  is the expected number of events in the  $i$ -th bin.

For the analysis of the event rate distributions, the expected number of events,  $\lambda_i$ , is corrected for the live time fraction. For example, when fitting the event rate distribution with an exponential function, the expectation is written as

$$\lambda_i = \epsilon_i \int_{(i-1)\Delta t}^{i\Delta t} N_0 \cdot e^{-\ln 2 t/T_{1/2}} dt \tag{5}$$

where  $\epsilon_i$  is the value in the  $i$ -th bin of the live time fraction distribution,  $\Delta t$  is the bin width,  $N_0$ , the initial event rate and  $T_{1/2}$ , the half life.

The spectral analysis was done by fitting the spectra of different contributions obtained from the MC simulations to the observed energy spectrum. The expected number of events in the  $i$ -th bin,  $\lambda_i$  is defined as the sum of the expected number of events from each model component in the  $i$ -th bin and is written as

$$\lambda_i = \sum_M \lambda_{i,M}, \tag{6}$$

where  $M$  corresponds to the simulated background components considered in the fit. The expectation from a model component in the  $i$ -th bin is defined as

$$\lambda_{i,M} = N_M \int_{\Delta E_i} f_M(E) dE \tag{7}$$

where  $f_M(E)$  is the normalized simulated energy spectrum of the component  $M$  and  $N_M$  is the scaling parameter, i.e., the integral of the spectrum in the fit window.

Global fits of the experimental spectra and fits of the event rate distributions were performed according to the procedure described above and using the Bayesian Analysis Toolkit BAT [29]. The prior probabilities of the parameters  $P_0(\lambda_M)$  are given as a flat distribution if not otherwise indicated.

### 5.2 $\alpha$ event rate analysis

The  $\alpha$  induced events in the energy range 3.5–7.5 MeV are expected to mainly come from  $\alpha$  emitting isotopes in the  $^{226}\text{Ra}$  decay chain, which can be broken at  $^{210}\text{Pb}$  and at  $^{210}\text{Po}$  with half lives of 22.3 yr and 138.4 days, respectively. An analysis of the time distribution is therefore used to infer the origin of these events.

If only  $^{210}\text{Po}$  is present as a contamination, the count rate in the energy region from 3.5 to 5.3 MeV (see Fig. 9) should decrease with a decay time expected from the half life of  $^{210}\text{Po}$ . Whereas an initial  $^{210}\text{Pb}$  surface contamination would cause an event rate in this energy interval appearing

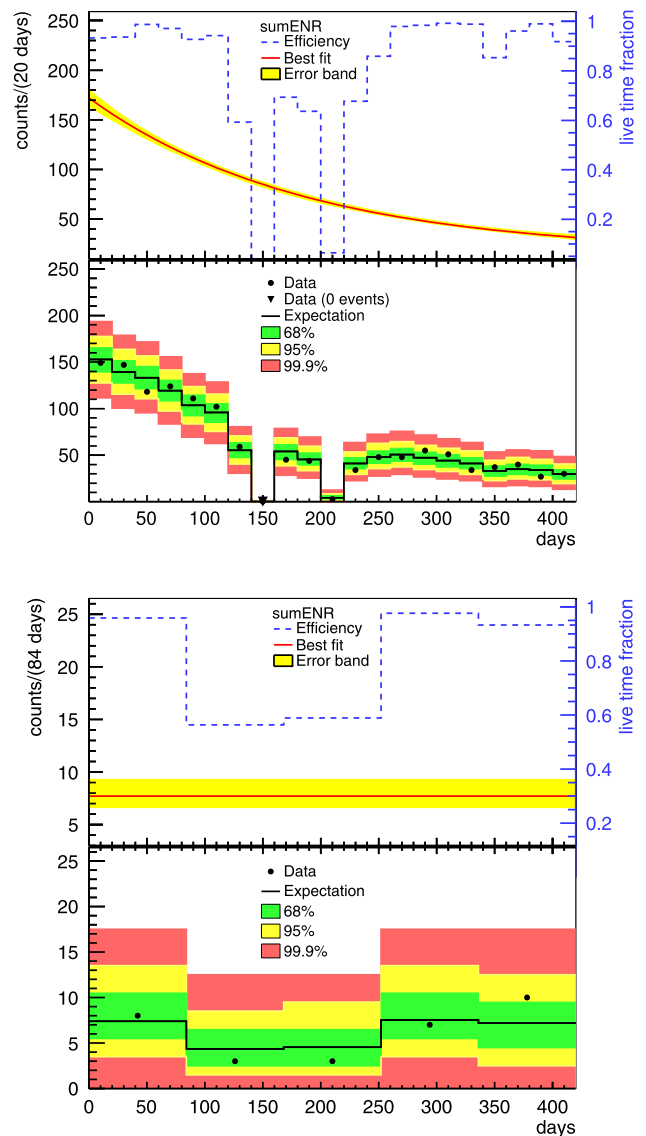


**Fig. 9** Results of fitting the event rate distributions for events in the 3.5–5.3 MeV range with an exponential plus constant rate model (top) and for the events in the 5.3–7.5 MeV range fitted with a constant rate model (bottom). The upper panels show the best fit model (red lines) with 68 % uncertainty (yellow bands) and the live time fraction distribution of the experiment (dashed blue line). The lower panels show the observed number of events (markers) and the expected number of events (black line) due to the best fit. The smallest intervals of 68, 95 and 99.9 % probability for the expectation are also shown in green, yellow and red regions, respectively [30]

constant in time, as the half life of  $^{210}\text{Pb}$  is much longer than the life time of the experiment. The event rate at energies  $E > 5.3$  MeV should appear constant in time in case events originate from the decay of  $^{226}\text{Ra}$  with a half life of  $T_{1/2} = 1600$  yr and its short lived daughters.

The *GOLD-coax* data set was analyzed using the statistical method described in Sect. 5.1. For the energy region 3.5 to 5.3 MeV two models were fitted to the event rate distributions: an exponentially decreasing rate and an exponentially

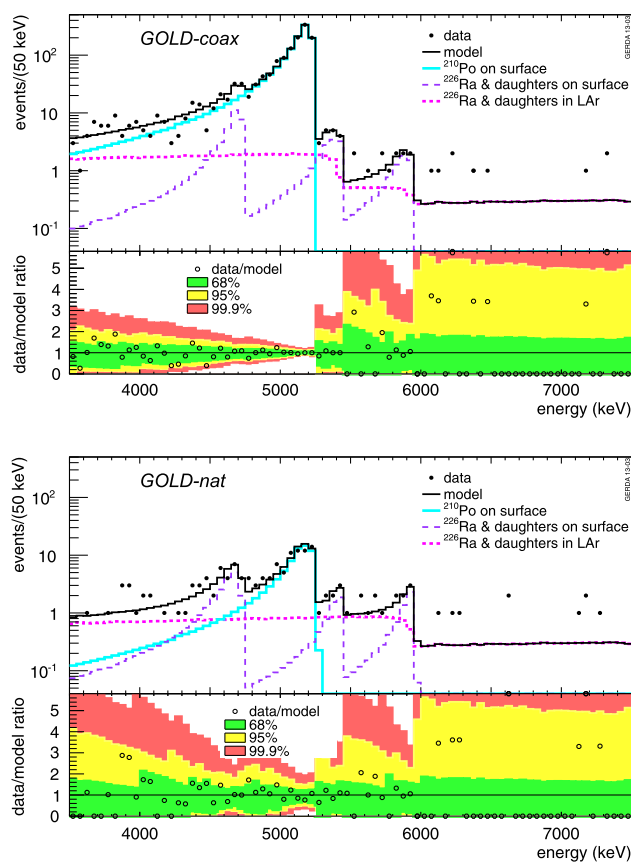
decreasing plus a constant rate. For the rate of events with  $E > 5.3$  MeV only a constant rate was fitted. The live time fraction as a function of time is taken into account in the analysis. A strong prior probability distribution for the half life parameter,  $P_0(T_{1/2})$ , is given as a Gaussian distribution with a mean value of 138.4 days and a standard deviation of 0.2 days for both models, to check the assumption of an initial  $^{210}\text{Po}$  contamination. The analysis was also performed by giving a non-informative prior, a flat distribution, on the half life parameter. For the energy range between 3.5 and 5.3 MeV both models describe the distribution adequately. The exponentially decreasing plus constant rate model is, however, clearly preferred as it results in a nine times higher p-value of 0.9. The rates derived from the fit are  $(0.57 \pm 0.16)$  cts/day for the constant term and  $(7.9 \pm 0.4)$  cts/day for the initial rate, exponentially decreasing with a half life of  $(138.4 \pm 0.2)$  days, according to the fit performed with the strong prior on the half life. The fit with non informative prior on the half life parameter results in a half life of  $(130.4 \pm 22.4)$  days, which is in very good agreement with the half life of  $^{210}\text{Po}$ . The constant event rate model for the events with  $E > 5.3$  MeV gives a very good fit as well and results in a count rate of  $(0.09 \pm 0.02)$  cts/day.

Figure 9 shows the observed event rate for both energy regions and the expectation due to the best fit event rate model together with the smallest intervals containing 68, 95 and 99.9 % probability for the expectation. The live time fraction for data taking was varying with time and is also shown. The observed exponential decay rate clearly shows that the majority of the observed  $\alpha$  events come from an initial  $^{210}\text{Po}$  contamination on the detector surfaces. The results of the time analysis show agreement with the assumed origins of the events.

### 5.3 Background components

#### 5.3.1 $^{226}\text{Ra}$ decay chain on and close to the detector surface

As demonstrated in Fig. 7 the maximal energy in the peak like structure resulting from an  $\alpha$  decay on the detector surface is very sensitive to the dead layer thickness. The  $^{210}\text{Po}$  peak structure around 5.3 MeV with high statistics in the *GOLD-coax* data set was used to determine the effective dead layer model. Spectra from  $^{210}\text{Po}$   $\alpha$  decay simulations on the  $\text{p}^+$  surface with different dead layer thicknesses were used to fit the spectrum in the energy region dominated by the  $^{210}\text{Po}$  peak, i.e. between 4850 and 5250 keV. The weight of each spectrum was left as a free parameter. A combination of the spectra for 300, 400, 500 and 600 nm dead layer thicknesses describes the observed peak structure well and results in a very good fit, whereas a spectrum with a single dead layer thickness does not give a sufficiently good fit. Consequently



**Fig. 10** The upper panels show the best fit model (black histogram) and observed spectrum (black markers) for the *GOLD-coax* (upper plots) and the *GOLD-nat* (lower plots) data sets. Individual components of the model are shown as well. The lower panels show the ratio of data and model and the smallest intervals of 68 % (green), 95 % (yellow) and 99.9 % (red) probability for the model expectation

the derived dead layer model was used for the later fits of  $\alpha$  induced spectra. Spectra with lower (down to 100 nm) and higher dead layer thicknesses (up to 800 nm) give insignificant contributions, if at all, to the overall spectrum.

In order to describe the whole energy interval dominated by  $\alpha$ -induced events, the simulated spectra of  $\alpha$  decays of  $^{210}\text{Po}$  as well as from  $^{226}\text{Ra}$  and its short lived daughter nuclei on the  $\text{p}^+$  surface and in LAr (see Table 5) were used to fit the energy spectrum between 3500 and 7500 keV. The number of events in the considered energy range was left as a free parameter for each  $\alpha$  component. The same analysis was repeated for different data sets. The best fit model together with the individual contributions and observed spectrum for the *GOLD-coax* and *GOLD-nat* data sets are shown in Fig. 10. While the surface decays alone can successfully describe the observed peak structures, they could not describe the whole spectrum. A contribution from an approximately flat component, like the spectra from  $\alpha$  decays in LAr, is needed in the model. All the data sets, and even the spectra of individual detectors can be very well described by

**Table 6** Number of events in the whole energy range (0.1–7.5 MeV) from each component of the  $\alpha$  model obtained for different data sets. Shown are the mode and the smallest 68 % probability intervals or 90 % quantiles of the marginalized distributions of the parameters. Note that while the marginalized distributions result in upper limits, the global best fits result in positive contributions

	Number of counts in the spectrum							
	<i>GOLD-coax</i>		<i>GOLD-nat</i>		<i>GOLD-hdm</i>		<i>GOLD-igex</i>	
$^{210}\text{Po p}^+$	1355	[1310, 1400]	76.5	[66, 88]	1285.5	[1240, 1320]	74.5	[65, 86]
$^{226}\text{Ra p}^+$	50.5	[36.0, 65.0]	27.5	[20, 36]	46.5	[35, 62]	8.5	[5, 13]
$^{222}\text{Rn p}^+$	24.5	[18, 33]	13.5	[9, 20]	23.5	[17, 32]	6.5	[3, 10]
$^{218}\text{Po p}^+$	13.5	[9.0, 19.0]	15.5	[10, 20]	13.5	[9, 19]	<6	
$^{214}\text{Po p}^+$		<10		<11		<9		<7
$^{226}\text{Ra LAr}$		<159.0		<45		<148		<26
$^{222}\text{Rn LAr}$		<64		<25		<52		<10
$^{218}\text{Po LAr}$		<30		<26		<30		<6
$^{214}\text{Po LAr}$	19.5	[10, 29]	16.5	[8, 27]	14.5	[8, 25]		<5

this model. Therefore, no further possible contributions from other  $\alpha$  sources are considered in the analysis of this energy range.

The number of expected  $\alpha$  induced events in the whole energy range (0.1–7.5 MeV) from each component of the model are listed in Table 6. In each subsequent decay in the chain the number of events measured is systematically reduced with respect to the mother nuclei for  $\text{p}^+$  surface decays. Due to having few events above 5.3 MeV, mostly only a limit could be derived for the components of decays in LAr. Nevertheless, a similar systematic decrease can be observed. The model for all data sets and also the model for individual detectors show the same effect. This could be explained by the removal of the mother nucleus from the surface by recoil with  $\approx 100$  keV. Since the range of  $\alpha$  particles in LAr and in Ge (DL) is only few  $\mu\text{m}$ , the detection efficiency of the  $\alpha$  particle emitted by the isotope that has recoiled from the surface can be reduced. However, the recoil of the nuclei away from the surface will practically not effect the detection efficiencies of  $\beta$  particles or  $\gamma$  rays, since they have significantly greater penetration depths in LAr. Therefore, decays of  $^{214}\text{Bi}$  in LAr in the vicinity of the surface ( $\mu\text{m}$ ) and decays directly on the  $\text{p}^+$  surface are expected to have very similar detection efficiencies and result in the same spectral shapes within uncertainties. Thus, for the rate of  $^{214}\text{Bi}$  decaying on the detector  $\text{p}^+$  surface a rate equal to the one of the  $^{226}\text{Ra}$  decays on the  $\text{p}^+$  surface as obtained by the  $\alpha$  model is assumed. In the background model this expectation is accounted for by putting a Gaussian prior probability on the number of  $^{214}\text{Bi}$  events on the  $\text{p}^+$  surface as described in the following section.

Figure 11 shows the number of observed events with energies  $>5.3$  MeV versus the number of expected events from the  $\alpha$  model excluding the contribution from  $^{210}\text{Po}$  in the energy range between 3.5 and 5.3 MeV for individual

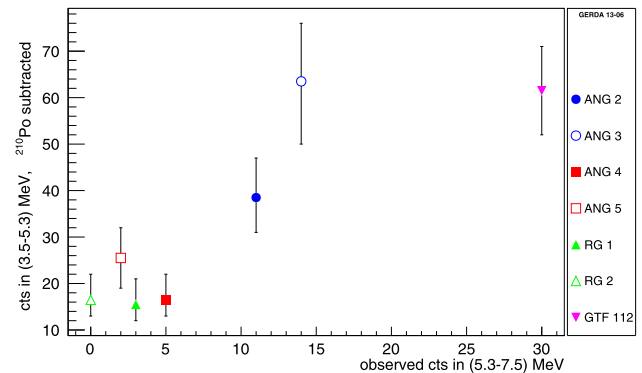


**Fig. 11** Number of observed events with energies  $>5.3$  MeV versus the number of events in the interval 3.5–5.3 MeV with the  $^{210}\text{Po}$  contribution subtracted according to the model for individual detectors

detectors. A correlation between the two numbers is visible, supporting the assumption that the events between 3.5 and 5.3 MeV that are not due to  $^{210}\text{Po}$  and events above 5.3 MeV are originating from the same source.

### 5.3.2 Additional relevant background components

The energy spectrum is described from 570 keV (from energies above the Q-value of the  $^{39}\text{Ar}$  decay) up to 7500 keV by considering all the background sources in the model that are expected to be present in the setup—namely,  $2\nu\beta\beta$  decay of  $^{76}\text{Ge}$ ,  $^{40}\text{K}$ ,  $^{60}\text{Co}$ ,  $^{228}\text{Th}$ ,  $^{228}\text{Ac}$ ,  $^{214}\text{Bi}$ ,  $^{42}\text{K}$  and  $\alpha$ -emitting isotopes in the  $^{226}\text{Ra}$  decay chain.

A minimum model was defined to fit the spectrum with a minimum number of expected contributions from sources close to the detector array. It contains the following components: the  $2\nu\beta\beta$  spectrum,  $^{40}\text{K}$ ,  $^{60}\text{Co}$ ,  $^{228}\text{Th}$ ,  $^{228}\text{Ac}$  and  $^{214}\text{Bi}$  in or on the detector assembly,  $^{42}\text{K}$  distributed homogeneously in LAr and the best fit  $\alpha$  model. For  $^{60}\text{Co}$  in ger-

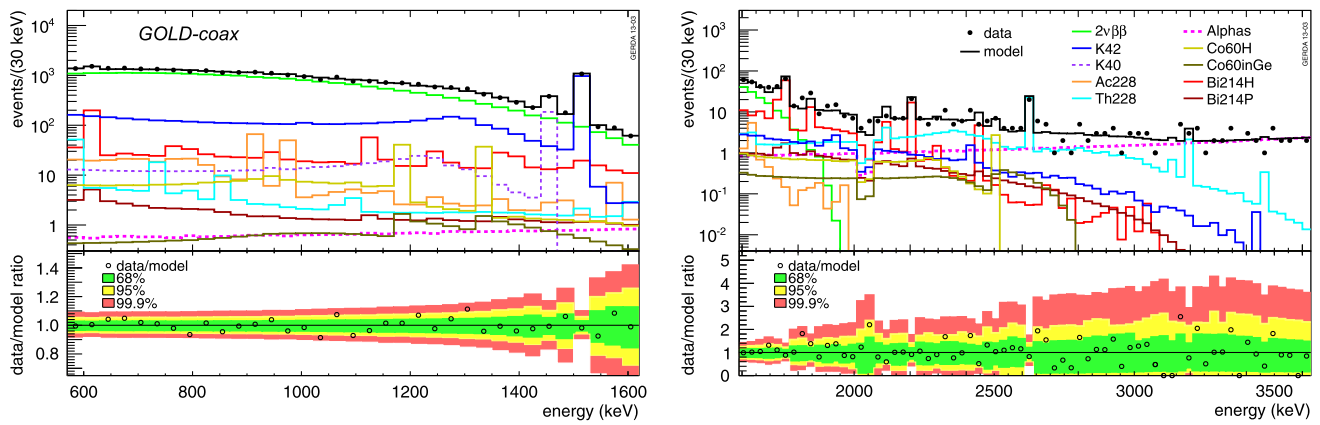


**Fig. 12** Background decomposition according to the best fit minimum model of the *GOLD-coax* data set. The *lower panel* in the plots shows the ratio between the data and the prediction of the best fit model together

with the smallest intervals of 68 % (green band), 95 % (yellow band) and 99.9 % (red band) probability for the ratio assuming the best fit parameters

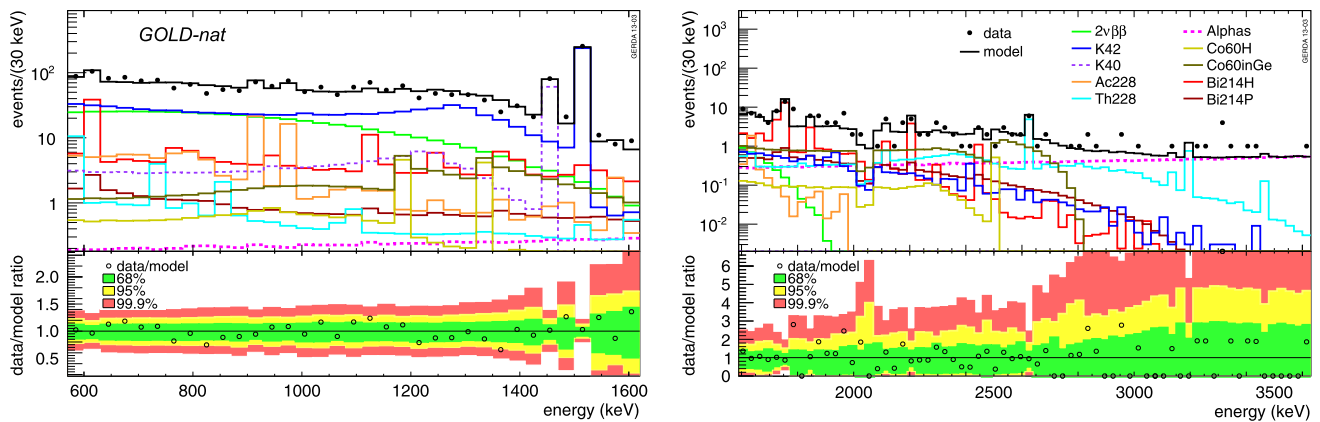


**Fig. 13** Same as in Fig. 12 for the *GOLD-nat* data set

manium a flat prior probability distribution is given to the number of expected events, allowing a maximum contribution of  $2.3 \mu\text{Bq}$  initial activity. This upper boundary is derived from the known activation history of the detectors with the assumption of 4 nuclei/(kg day) cosmogenic production rate [11].  $^{214}\text{Bi}$  on the  $p^+$  surface is given a Gaussian prior probability due to the expected  $^{226}\text{Ra}$  activity on  $p^+$  surface derived from the  $\alpha$  model, with a mean equal to the marginalized mode and a  $\sigma$  corresponding to the smallest 68 % interval of the parameter.

The maximum model considers additional contributions. These are:  $^{42}\text{K}$  on the  $p^+$  and  $n^+$  surfaces of the detectors,  $^{228}\text{Th}$  in or on the radon shroud and the heat exchanger,  $^{228}\text{Ac}$  and  $^{214}\text{Bi}$  in or on the radon shroud and  $^{214}\text{Bi}$  in the LAr close to  $p^+$  surfaces of the detector. The number of expected events from all the additional components are left as free parameters, i.e. they are not given any informative priors.

#### 5.4 Fit results

The minimum and the maximum fits were performed in the energy range from 570 to 7500 keV with a 30 keV binning using the statistical method given in Sect. 5.1.

Both models describe the data very well resulting in reasonable p-values with no clear preference for one model. Figs. 12 and 13 show the minimum model fit to the *GOLD-coax* and the *GOLD-nat* data sets in the energy regions between 570 and 1620 keV and between 1580 and 3630 keV. The lower panels in the plots show the data to model ratio (markers) and the smallest intervals containing 68, 95 and 99.9 % probability for the ratio assuming the best fit parameters in green, yellow and red bands, respectively [30]. The data is within reasonable statistical fluctuations of the expectations.

From the minimum and the maximum fit models, activities of contaminations of some of the components with different



**Table 7** Activities of the individual contaminations of different hardware components derived from the global models of different data sets. The location of the sources is also indicated. The numbers are according to the best fit model. The uncertainty interval obtained as the smallest 68 % interval of the marginalized distributions of the parameters are given as well. Limits are given with 90 % C.L. Also the activities as derived from the coincident sum spectra (see Sect. 7) are shown

Source	Location	Units	<i>GOLD-coax</i>		<i>GOLD-nat</i>	<i>GOLD-coax</i>
			Minimum	Maximum	Minimum	Coincident
$^{40}\text{K}^c$	det. assembly	$\mu\text{Bq/det.}$	152 [136, 174]	151 [136, 174]	218 [188, 259]	252 [164, 340]
$^{42}\text{K}^c$	LAr	$\mu\text{Bq/kg}$	106 [103, 111]	91 [72, 99]	98.3 [92, 108]	168 [150, 186]
$^{42}\text{K}^c$	$p^+$ surface	$\mu\text{Bq}$		11.6 [3.1, 18, 3]		
$^{42}\text{K}^c$	$n^+$ surface	$\mu\text{Bq}$		4.1 [1, 2, 8.5]		
$^{60}\text{Co}^c$	det. assembly	$\mu\text{Bq/det.}$	4.9 [3.1, 7.3]	3.2 [1.6, 5.6]	2.6 [0, 6.0]	5.0 [2.5, 7.5] <sup>b</sup>
$^{60}\text{Co}^c$	Germanium	$\mu\text{Bq}$	>0.4 <sup>a</sup>	>0.2 <sup>a</sup>	6 [3.0, 8.4]	
$^{214}\text{Bi}^c$	det. assembly	$\mu\text{Bq/det.}$	35 [31, 39]	15 [3.7, 21.1]	34.1[27.3, 42.1]	40 [28, 52]
$^{214}\text{Bi}^c$	LAr close to $p^+$	$\mu\text{Bq/kg}$		<299.5		
$^{214}\text{Bi}^m$	Radon shroud	mBq		<49.9		
$^{214}\text{Bi}^c$	$p^+$ surface	$\mu\text{Bq}$	2.9 [2.3, 3.9] <sup>a</sup>	3.0 [2.1, 4.0] <sup>a</sup>	1.6 [1.2, 2.1] <sup>a</sup>	
$^{228}\text{Th}^c$	det. assembly	$\mu\text{Bq/det.}$	15.1 [12.7, 18.3]	5.5 [1.8, 8.8]	15.7 [10.0, 25.0]	9.4 [7.9, 10.9]
$^{228}\text{Ac}^c$	det. assembly	$\mu\text{Bq/det.}$	17.8 [10.0, 26.8]	<15.7	25.9 [16.7, 36.7]	33 [18, 48]
$^{228}\text{Th}^m$	Radon shroud	mBq		<10.1		
$^{228}\text{Ac}^m$	Radon shroud	mBq		91.5 [27, 97]		
$^{228}\text{Th}^f$	Heat exchanger	Bq		<4.1		

Source distance: *c* close (<2 cm); *m* medium (2–30 cm); *f* far (>30 cm)

<sup>a</sup> Prior: discussed in the text

<sup>b</sup> Obtained from coincident spectrum with histogram entries for each detector event separately

radioactive isotopes have been derived and are summarized in Table 7.

A comparison of the resulting activities in Table 7 with the known inventory of radio contaminations shown in Table 2 shows that all contaminations expected from screening are seen in the background spectra. However, the activities identified by screening measurements are not sufficient to explain the total background seen. The minimum model describes the background spectrum well without any medium distance and distant contaminations. Also if medium distance and distant sources are added, the largest fraction to the background comes from close sources, especially on the  $p^+$  and  $n^+$  surfaces. Note, that the activity obtained for  $^{42}\text{K}$  and hence for the  $^{42}\text{Ar}$  contamination of LAr is higher than the previously most stringent limit reported in Ref. [31].

In the maximum model, strong correlations are found between several background sources. Contaminations of  $^{42}\text{K}$  on the  $n^+$  surface and in LAr can not be distinguished. Similarly, the model has no distinction power between contaminations of the radon shroud, the heat exchanger and the detector assembly with  $^{214}\text{Bi}$ ,  $^{228}\text{Th}$  and  $^{228}\text{Ac}$ . This explains the differences of the derived activities in the two models. The main difference between minimum and maximum models is the number of events on the  $p^+$  surface of the detectors.

A fit of the background model has also been made to the *SILVER-coax* data set. Its overall spectral shape can only be

described sufficiently well, if either an additional  $^{42}\text{K}$  contamination of the  $p^+$  surface and/or an additional  $^{214}\text{Bi}$  contamination of the LAr is assumed. Both additional contaminations seem plausible after a modification of the experimental surrounding like the insertion of BEGe detectors to the cryostat.

## 6 Background model for BEGe detectors

An equivalent procedure as for the coaxial detectors was used to model the energy spectrum observed for the *SUMbege* data set. Since the exposure collected with the BEGe detectors is much smaller than for the coaxial data set, only a qualitative analysis is possible for this data set. The lower mass of the BEGe detectors with respect to the coaxial detectors reduces the detection efficiency for full energy peaks. Hence, fewer  $\gamma$  lines are positively identified in the BEGe spectrum. This makes it even more difficult to establish and to constrain possible background components.

The contributions to the BEGe background model were simulated using an implementation of the GERDA Phase I detector array containing the three coaxial detector strings and an additional string with the five BEGe detectors. The  $n^+$  dead layer thicknesses used in the MC are listed in Table 1. The effective  $p^+$  dead layer thickness was set to 600 nm.

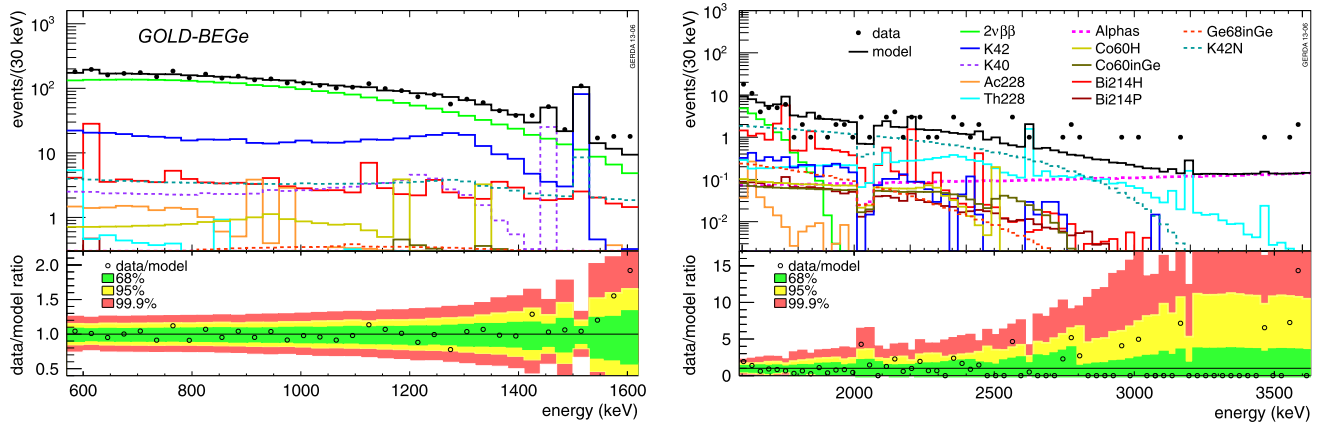


Fig. 14 Same as in Fig. 12 for the SUM-bege data set

The minimum model contributions were considered. Additionally, two contributions were added to the BEGe model:  $^{68}\text{Ge}$  decays in germanium and  $^{42}\text{K}$  decays on the  $n^+$  surface. A contribution from  $^{68}\text{Ge}$  is expected due to cosmogenic activation above ground, analogously to  $^{60}\text{Co}$  in germanium. Due to the rather short half life of 271 days the  $^{68}\text{Ge}$  contribution can be neglected for the coaxial detectors, which have been stored underground for several years. For the newly produced BEGe detectors, however, these decays and the subsequent decay of  $^{68}\text{Ga}$  have to be taken into account. The contribution from  $^{42}\text{K}$  decays on the  $n^+$  surface, on the other hand, is enhanced with respect to the coaxial detectors due to the thinner dead layer and has to be taken into account for the model. The  $n^+$  surface dead layer is partially active [32], which in particular affects the detection efficiency for surface  $\beta$  interactions. Thus, the MC simulation used for  $^{42}\text{K}$  on  $n^+$  surface included an approximation of this effect. 40 % of the dead layer thickness (as stated in Table 1) has been modeled with zero charge collection efficiency, the other part with a linearly increasing charge collection efficiency from 0 to 100 %.

The contributions of  $^{60}\text{Co}$  and  $^{68}\text{Ge}$  to the model are limited to 0.05 and 0.32 cts/day, respectively. The upper values for these cosmogenically produced isotopes are derived from an assumed activation rate for these isotopes according to Ref. [27] and the known histories of exposure to cosmic rays of the individual detectors.

The procedure to obtain the best fit was equivalent to the model definition of the coaxial detectors. The best fit model for BEGe detectors is shown in Fig. 14. Around  $Q_{\beta\beta}$  the largest contribution arise from  $^{42}\text{K}$  on the  $n^+$  surfaces (see last column of Table 10).

The presented BEGe background model is consistent with a background decomposition obtained by pulse shape discrimination of the data [10].

Table 8  $T_{1/2}^{2\nu}$  values derived from different background models. The uncertainties are those from the fit parameters and do not include systematic uncertainties

Model	$\mathcal{E}$ [kg yr]	$T_{1/2}^{2\nu} \times 10^{21}$ yr
GOLD-coax minimum	15.40	$1.92^{+0.02}_{-0.04}$
GOLD-coax maximum	15.40	$1.92^{+0.04}_{-0.03}$
GOLD-nat minimum	3.13	$1.74^{+0.48}_{-0.24}$
SUM-BEGe	1.80	$1.96^{+0.13}_{-0.05}$
Analysis in Ref. [20]	5.04	$1.84^{+0.09}_{-0.08}$ fit $^{+0.11}_{-0.10}$ syst

### 7 Cross checks of the background model

The background model developed has some predictive power that can be checked with the available data. This section describes cross checks performed on the background model.

#### 7.1 Half life derived for $2\nu\beta\beta$ decay

From the best fit models the resulting half life  $T_{1/2}^{2\nu}$  for  $2\nu\beta\beta$  decay can be extracted.  $T_{1/2}^{2\nu}$  is calculated using the relation

$$T_{1/2}^{2\nu} = \frac{\ln 2 \cdot N_A}{m_{enr}} \frac{\mathcal{E}}{N_{model}} \langle \varepsilon^{2\nu} \rangle, \tag{8}$$

where  $N_{model}$  is the best fit number of  $2\nu\beta\beta$  decays derived from the individual model. The efficiency  $\langle \varepsilon^{2\nu} \rangle$  is given by the weighted detection efficiency of  $2\nu\beta\beta$  decays in the fit range,  $\varepsilon_i$ ,

$$\langle \varepsilon^{2\nu} \rangle = \frac{\sum_i f_{av,i} f_{76,i} M_i t_i \varepsilon_i}{\mathcal{E}}. \tag{9}$$

Table 8 gives the half lives extracted from the different background models. All results are consistent with the earlier GERDA  $2\nu\beta\beta$  analysis [20] within the uncertainties. Note,

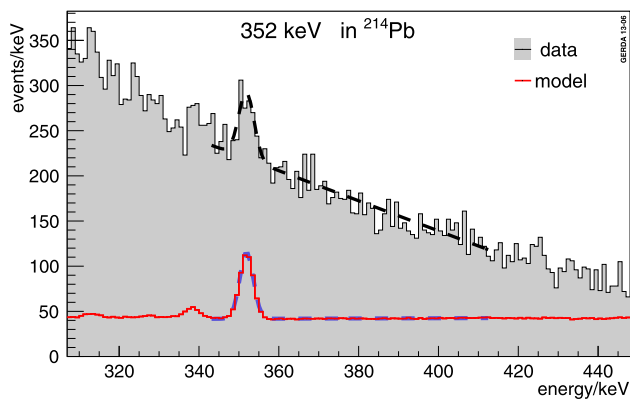


**Fig. 15** Energy spectrum of the *GOLD-coax* data set (filled histogram) and the minimum model prediction (red histogram). The data and the model spectrum are fitted with a Gaussian plus linear background (dashed lines)

that a three times larger exposure was available for this analysis as compared to the analysis in Ref. [20] while systematic uncertainties are not considered.

## 7.2 Intensities of $\gamma$ lines

At energies below 600 keV the energy spectrum is dominated by  $^{39}\text{Ar}$  with an activity of  $A = [1.01 \pm 0.02(\text{stat}) \pm 0.08(\text{syst})]$  Bq/kg [33] homogeneously distributed in LAr. This part of the spectrum has not been included into the background fit to avoid uncertainties due to the  $n^+$  dead layer thickness and the theoretical shape of the beta decay spectrum. A strong  $\gamma$  line at 352 keV is, however, expected from decays of  $^{214}\text{Bi}$  in the vicinity of the detectors. The intensity of this line depends strongly on the distance of the  $^{214}\text{Bi}$  contamination from the detectors. Hence, this cross check can give a hint on how realistic the assumed distribution of the  $^{214}\text{Bi}$  contamination is. The minimum (maximum) model predicts  $20.1^{+2.6}_{-2.2}$  ( $17.5^{+7.0}_{-13.3}$ ) counts/(kg yr) in the peak while a fit of a Gaussian plus a linear background to the data gives  $20.4^{+4.4}_{-4.2}$  counts/(kg yr) for the *GOLD-coax* data set. Figure 15 shows the energy spectrum of the *GOLD-coax* data set in the energy region between 310 and 440 keV. The Gaussian plus linear background fit to the data as well as the minimum model prediction without the  $^{39}\text{Ar}$  contribution dominating the spectrum in this energy region is shown. For the *GOLD-nat* data set the minimum model prediction of  $22.1^{+5.2}_{-4.4}$  counts/(kg yr) is also consistent with the observed  $25.6^{+8.5}_{-7.5}$  counts/(kg yr). This cross check makes it possible to distinguish between the locations of  $^{214}\text{Bi}$  contaminations if it is assumed that the decays of  $^{214}\text{Bi}$  and  $^{214}\text{Pb}$  happen at the same location. It excludes the results for  $^{214}\text{Pb}$  contamination in or on the radon shroud as the best fit maximum model for the *GOLD-nat* data set predicts. This model predicts only  $4.6^{+1.4}_{-1.5}$  counts/(kg yr). This cross check confirms

the indication from the background model that close sources are responsible for most of the  $^{214}\text{Bi}$  background contribution.

As the fit has been performed with a binning larger than the energy resolution of the detectors, the information from the line intensities is not maximized in the fitting procedure. Hence, it is instructive to cross check the line intensities obtained from fitting the peaks with a Gaussian plus linear background in the different data sets with the expectation from the models. Table 9 compares the  $\gamma$ -line intensities from the minimum and maximum models to those obtained from a fine binned analysis, i.e. a fit to data. Note, that for some of the  $\gamma$  peaks no fit could be performed due to limited number of events in the peak region or the low intensity of the  $\gamma$  line compared to the other background contributions. In those cases the number of counts in the  $\pm 3\sigma$  energy range around the peak positions were used. The background has been estimated according to the continuum seen in the  $\pm 5\sigma$  side bands at lower and higher energies around the peak. A narrower side band is used when there is a second line close to the peak. The intensities of the  $\gamma$  lines are obtained by marginalizing the posterior probability distribution of the signal rate. The uncertainties on the predicted rate by the global models are due to the fit uncertainty on the parameters of the model components that give contribution to the  $\gamma$ -ray line. The statistical uncertainties due to the simulated number of events is on the order of 0.1 %, i.e. negligible compared to the fit uncertainty. There is excellent agreement between the numbers from the global analysis and those from the fine-binned analysis.

## 7.3 Stability of the fit

To check for stability, the fits were performed using different binnings. As the energy resolution of the detectors is around 4.5 keV at  $Q_{\beta\beta}$  and the calibration at higher energies  $E > 5$  MeV, relevant for the  $\alpha$  model is precise to about 10 keV, the lowest binning chosen was 10 keV. Also a 50 keV binning was performed. The activities of different components derived from the fits with different binnings do not vary outside the uncertainties given for the 30 keV binning fits.

Additionally it was checked whether the overall goodness of fit and the predicted BI and individual contributions in the region of interest changes if biases are introduced to the fits by single strong assumptions on individual background components.

Minimum model fits for the *GOLD-coax* and *GOLD-nat* data sets were performed with the following individual modifications:  $^{228}\text{Th}$  and  $^{228}\text{Ac}$  are only in or on the radon shroud; no  $^{214}\text{Bi}$  is present on the  $p^+$  surface;  $^{42}\text{K}$  is only on the  $p^+$  surface;  $^{42}\text{K}$  is present on the  $p^+$  surface;  $^{60}\text{Co}$  is only inside the crystal,  $^{60}\text{Co}$  is only inside the detector assembly. Except

**Table 9** Count rates of background  $\gamma$  lines for the *GOLD-coax* and *GOLD-nat* data sets obtained by the global analysis (minimum and maximum model) and with a fine binned fit of the data. Upper limits correspond to 90 % credibility interval. The central value is the mode of the posterior probability distribution function and the confidence intervals account for the smallest interval containing 68 % probability

Isotope	Energy [keV]	Rate [cts/(kg yr)]					
		<i>GOLD-coax</i>			<i>GOLD-nat</i>		
		Global analysis (min. fit)	Global analysis (max. fit)	Fit to data	Global analysis (min. fit)	Global analysis (max. fit)	Fit to data
$^{40}\text{K}$	1460.8	11.9 [10.6, 13.6]	11.8 [10.6, 13.6]	13.6 [12.5, 15.0]	19.4 [16.7, 23.0]	19.8 [16.7, 23.1]	18.3 [15.7, 21.4]
$^{42}\text{K}$	1524.7	61.2 [59.3, 63.8]	61.4 [48.5, 66.2]	60.3 [58.1, 62.5]	75.0 [70.2, 82.4]	75.6 [49.1, 78.3]	73.8 [69.1, 80.1]
$^{60}\text{Co}$	1173.2	2.5 [1.6, 3.7]	1.6 [0.6, 2.9]	4.2 [2.8, 5.6]	2.0 [0.1, 4.6]	1.9 [0.1, 3.2]	<3.8
	1332.3	2.3 [1.4, 3.4]	1.5 [0.5, 2.6]	<1.6	1.9 [0.1, 4.4]	1.7 [0.1, 2.8]	3.3 [1.6, 5.2]
$^{228}\text{Ac}$	911.2	3.8 [2.2, 5.8]	3.4 [1.0, 3.6]	3.9 [2.2, 5.6]	6.1 [3.9, 8.6]	5.4 [0.5, 9.8]	4.9 [2.7, 7.3]
	969.0	2.7 [1.5, 4.1]	2.8 [0.8, 2.8]	3.5 [1.8, 5.0]	4.4 [2.8, 6.2]	3.9 [0.4, 7.1]	4.8 [2.6, 7.4]
$^{208}\text{Tl}$	583.2	2.9 [2.5, 3.5]	1.3 [0.3, 2.0]	3.9 [1.8, 5.7]	3.0 [1.8, 4.7]	<0.9	2.5 [0.4, 4.6]
	2614.5	1.4 [1.2, 1.7]	1.0 [0.2, 1.5]	1.2 [0.9, 1.5]	1.5 [0.9, 2.4]	1.5 [0.0, 6.7]	1.4 [0.6, 2.3]
$^{214}\text{Pb}$	351.9	20.1 [17.9, 22.7]	17.5 [4.2, 24.5]	20.4 [16.2, 24.8]	22.1 [17.7, 27.3]	4.6 [3.1, 6.0]	25.6 [18.1, 34.1]
$^{214}\text{Bi}$	609.3	11.2 [10.0, 12.6]	8.0 [2.0, 11.2]	10.0 [8.0, 12.3]	11.2 [9.0, 13.8]	6.5 [4.6, 8.6]	7.6 [4.8, 11.0]
	1120.3	2.6 [2.3, 2.9]	1.8 [0.4, 2.5]	<3.1	2.6 [2.1, 3.2]	3.0 [2.1, 3.9]	4.0 [1.8, 6.3]
	1729.6	1.0 [0.9, 1.1]	1.0 [0.2, 1.4]	0.5 [0.2, 0.9]	1.3 [1.0, 1.6]	0.8 [0.5, 1.1]	0.9 [0.3, 1.]
	1764.5	3.6 [3.2, 4.1]	2.7 [0.7, 3.8]	3.1 [2.6, 3.7]	4.1 [3.3, 5.1]	3.7 [2.5, 4.9]	3.5 [2.4, 5.0]
	1847.4	0.6 [0.5, 0.7]	0.6 [0.1, 0.8]	0.6 [0.3, 1.0]	0.7 [0.6, 0.9]	0.5 [0.3, 0.6]	1.2 [0.5, 2.1]
	2204.2	1.0 [0.9, 1.1]	0.8 [0.2, 1.1]	0.8 [0.5, 1.2]	1.2 [1.0, 1.5]	1.3 [0.9, 1.7]	0.8 [0.2, 1.6]
	2447.9	0.3 [0.27, 0.34]	0.2 [0.05, 0.3]	0.2 [0.1, 0.4]	0.3 [0.2, 0.4]	0.4 [0.3, 0.5]	<1.8

for the unrealistic assumption that all  $^{42}\text{K}$  comes from  $p^+$  surface contaminations all fits describe the measured spectrum reasonably well.

The prediction for the BI at the region of interest varies by 10 % between the different models for the *GOLD-coax* data set and by 15 % for the *GOLD-nat* data set.

The predictions for the activities of the individual components of the different models are consistent within the 68 % uncertainty range quoted in Table 7.

#### 7.4 BiPo coincidences

An important contribution to the background model are surface events from  $^{226}\text{Ra}$  daughters. These include the decays of  $^{214}\text{Bi}$  and  $^{214}\text{Po}$ .  $^{214}\text{Po}$  has a half life of only 164.4  $\mu\text{s}$ . Hence, a number of events is expected where a low energy event from the  $^{214}\text{Bi}$  decay is followed by a high energy  $\alpha$  event from the  $^{214}\text{Po}$  decay in the same detector, a BiPo tag. The data reduction includes cuts that remove pile up events. As the half life of  $^{214}\text{Po}$  is of the order of the decay time of the preamplifier signal, the analysis is not tailored to reconstruct typical BiPo events. Hence it is difficult to quantify precisely the efficiency for this tag. Nevertheless, for the purpose of a qualitative statement an order of magnitude guess is made: An efficiency of 50 % is assumed for the BiPo recog-

nition efficiency. Using the number for the *GOLD-coax* data set obtained by the marginalized probability density function of the fit the number of detected  $^{218}\text{Po}$  surface events is 13.5 being reduced to approximately seven events from  $^{214}\text{Bi}$  decays on the surface that can lead to energy deposition in the detector active volume (the decrease being due to the decay nucleus recoiling away from the surface). With an efficiency of the order of 50 % to detect the BiPo tag only roughly 3 to 4 BiPo events are expected. In the *GOLD-coax* data set in total 5 events have been found (2 in ANG 2, 2 in ANG 3 and 1 in RG 1) that satisfy the criteria for a BiPo tag.

#### 7.5 Recognition of $p^+$ events

A mono-parametric pulse shape analysis technique for the identification of surface interactions on the  $p^+$  electrode of coaxial detectors has been recently developed and applied on Phase I data [34]. The method is based on a cut on the rise time of the charge pulses computed between 5 and 50 % of the maximum amplitude. The cut level is calibrated on experimental data using the pure sample of high-energy  $\alpha$ -induced events.

The analysis has been extended to the entire *GOLD-coax* data set. Fixing the cut to accept 95 % of the events occurring in the proximity of the  $p^+$  electrode, in the energy region of

interest 43 % of the events survive the cut. Part of the events surviving the cut is expected to be due to  $\gamma$  interactions in the proximity of the  $p^+$  surface. Applying the corrections described in Ref. [34], the total amount of  $\alpha$  and  $\beta$  induced events on the  $p^+$  electrode is estimated to be between 15 and 35 % of the number of events in the energy region of interest.

This result is consistent with the number of decays on the  $p^+$  surface predicted by the minimal model ( $20.5 \pm 2.7$  %), given by the  $\alpha$  emitting isotopes plus  $^{214}\text{Bi}$ . It is slightly lower compared to the maximal background model that requires 50 % considering  $\alpha$ ,  $^{214}\text{Bi}$  and  $^{42}\text{K}$  on the  $p^+$  surface.

## 7.6 Coincident spectrum

As a large fraction of the contaminations are, according to the background model(s), located inside the detector array (i.e. in the detector assembly, or in LAr close to the surfaces of the detectors), a significant number of events are expected to have coincident hits in two detectors. The efficiency to detect coincident events is expected to be increased with respect to single  $\gamma$  emitters for decays of isotopes with emission of multiple  $\gamma$  rays such as  $^{42}\text{K}$ ,  $^{60}\text{Co}$ ,  $^{214}\text{Bi}$  and  $^{208}\text{Tl}$ . Coincident spectra are, thus, sensitive to differences in source locations.

A sum coincidence spectrum was produced for the *GOLD-coax* data set by summing the energies of all detectors in an event and filling the corresponding bin of the histogram. Also a single coincidence spectrum was produced by filling the corresponding bin of the histogram for each individual detector separately.

The same procedure as for the minimum fit model (see Sect. 5) was applied to get best fit coincidence models for the single and sum spectra. The results for the activities obtained from the minimum model best fit to the sum spectrum (except for  $^{60}\text{Co}$ , where the single spectrum was used) are summarized in Table 7. The obtained activities from coincident and single detector spectra are consistent with each other. Note, that the simulations were not tuned for the coincidence analysis. The background source distribution was simplified in the simulation, while small changes in source location, especially within the detector array, can have significant effects on the coincidence efficiencies. The fact that the  $^{42}\text{K}$  activity derived from the coincidence fit is slightly higher than for the minimum and maximum models of the *GOLD-coax* and *GOLD-nat* data sets may be a hint that the distribution of  $^{42}\text{K}$  in LAr is not homogeneous. The consistency between the derived activities from coincident and single detector spectra support the result of the background model that the spectrum around  $Q_{\beta\beta}$  is dominated by contaminants close to the detectors.

## 8 Background prediction at $Q_{\beta\beta}$ and expected sensitivity for GERDA Phase I

### 8.1 Background prediction at $Q_{\beta\beta}$

The background models obtained by global fits in the 570–7500 keV region allow to predict the individual background contributions and the total background at  $Q_{\beta\beta}$ . Table 10 lists the predictions for the BI from different contributions in a 10 keV window for coaxial detectors and in a 8 keV window for BEGe detectors around  $Q_{\beta\beta}$  for different data sets. The results obtained from the best fit parameters are quoted together with the smallest 68 % interval of the marginalized distributions of the parameters. If the maximum of the marginalized distribution is at zero a 90 % upper limit is given. For the case of an internal  $^{60}\text{Co}$  contamination a 90 % lower limit is given, because a higher contamination gives a better fit, however, is constrained by prior knowledge of above ground exposure to cosmic rays. According to the models the main contributions to the background at  $Q_{\beta\beta}$  are due to the  $\alpha$ -emitting isotopes in the  $^{226}\text{Ra}$  decay chain,  $^{42}\text{K}$ ,  $^{60}\text{Co}$ ,  $^{214}\text{Bi}$  and  $^{228}\text{Th}$ . The fraction with which each component contributes depends on the assumed source location.

Table 10 also lists BIs expected from the screening measurements as reported in Table 2. The BIs due to the individual identified components do not match well with the BIs derived from the background model, indicating that unidentified close-by  $^{214}\text{Bi}$  and  $^{228}\text{Th}$  contributions have to be present.

Figure 16 shows the best fit minimum and maximum models and the individual contributions together with the observed spectrum around  $Q_{\beta\beta}$  for the *GOLD-coax* data set. The spectral shapes of the best fit models are constant around  $Q_{\beta\beta}$ . No peaks are predicted in the blinded regions. This indicates that the BI at  $Q_{\beta\beta}$  can be estimated by interpolating the results of a fit to the observed number of events outside the signal search window. The window to be used for this estimation is chosen as sum of the 1930–2019, 2059–2099, 2109–2114 and 2124–2190 keV intervals for a total width of 200 keV. The BI evaluation window excludes the central 40 keV window around  $Q_{\beta\beta}$  and the regions within  $\pm 5$  keV from the  $\gamma$  lines expected from the background model—namely, single escape peak from  $^{208}\text{Tl}$  at 2104 keV and the  $^{214}\text{Bi}$   $\gamma$  line at 2119 keV. The resulting background indices from the interpolation are listed in Table 11 for different data sets together with the prediction of the background models for comparison. The lower panels of the plots in Fig. 16 demonstrate that the background model can be described by a constant in the BI evaluation windows. The difference in the resulting BI is less than 1 % if a linear instead of a constant distribution is assumed. The statistical uncertainty for the approximation of the BI by an interpolation is of the same size as the systematic uncertainty expected by the model.

**Table 10** The total BI and individual contributions in 10 keV (8 keV for BEGes) energy window around  $Q_{\beta\beta}$  for different models and data sets. Given are the values due to the global mode together with the uncertainty intervals obtained as the smallest 68 % interval of the marginalized distributions. Limits are given with 90 % C.L. For details see the text

Component	Location	BI $10^{-3}$ cts/(keV kg yr)								Exp. from screening
		<i>GOLD-coax</i>				<i>GOLD-nat</i>		<i>SUM-bege</i>		
		Minimum model		Maximum model		Minimum model		Minimum + n <sup>+</sup>		
Total		18.5	[17.6, 19.3]	21.9	[20.7, 23.8]	29.6	[27.1, 32.7]	38.1	[32.2, 43.3]	
<sup>42</sup> K	LAr homogeneous	3.0	[2.9, 3.1]	2.6	[2.0, 2.8]	2.9	[2.7, 3.2]	2.0	[1.8, 2.3]	–
<sup>42</sup> K	p <sup>+</sup> surface			4.6	[1.2, 7.4]					–
<sup>42</sup> K	n <sup>+</sup> surface			0.2	[0.1, 0.4]			20.8	[6.8, 23.7]	–
<sup>60</sup> Co	det. assembly	1.4	[0.9, 2.1]	0.9	[0.3, 1.4]	1.1	[0.0, 2.5]		<4.7	–
<sup>60</sup> Co	Germanium	0.6	>0.1 <sup>a</sup>	0.6	>0.1 <sup>a</sup>	9.2	[4.5, 12.9]	1.0	[0.3, 1.0]	–
<sup>68</sup> Ge	Germanium							1.5	(<6.7)	–
<sup>214</sup> Bi	det. assembly	5.2	[4.7, 5.9]	2.2	[0.5, 3.1]	4.9	[3.9, 6.1]	5.1	[3.1, 6.9]	≈2.8
<sup>214</sup> Bi	LAr close to p <sup>+</sup>			3.1	<4.7					<0.7
<sup>214</sup> Bi	p <sup>+</sup> surface	1.4	[1.0, 1.8] <sup>a</sup>	1.3	[0.9, 1.8] <sup>a</sup>	3.7	[2.7, 4.8] <sup>a</sup>	0.7	[0.1, 1.3] <sup>a</sup>	–
<sup>214</sup> Bi	radon shroud			0.7	<3.5					–
<sup>228</sup> Th	det. assembly	4.5	[3.9, 5.4]	1.6	[0.4, 2.5]	4.0	[2.5, 6.3]	4.2	[1.8, 8.4]	<0.3
<sup>228</sup> Th	radon shroud <sup>b</sup>			1.7	<2.9					≈1.0
$\alpha$ model	p <sup>+</sup> surface and LAr close to p <sup>+</sup>	2.4	[2.4, 2.5]	2.4	[2.3, 2.5]	3.8	[3.5, 4.2]	1.5	[1.2, 1.8]	–

<sup>a</sup> Prior: discussed in Sect. 5

<sup>b</sup> Representing all distant sources including the heat exchanger, the wall of the steel cryostat and the calibration source at the bottom of the tank

The global fits were performed by excluding the central 40 keV region around  $Q_{\beta\beta}$  which was completely blinded until May 2013. Thereafter, a 30 keV (32 keV) window was opened for analysis by keeping the central 10 keV (8 keV) window still blinded for the enriched coaxial (BEGe) detectors. The natural detector GTF 112 was completely unblinded. The first step of unblinding gives the possibility to compare the model predictions to the observed number of events in those regions as a consistency check for the model. Table 11 also lists the predicted and observed number of events in these energy regions for different data sets. In total 13 events were observed in the unblinded 30 keV window of the *GOLD-coax* data set. The predictions in this window were 8.6 events from minimum and 10.3 events from maximum model. The probability to observe 13 events or more given the predictions are 10 and 24 %, respectively. In the *GOLD-nat* data set 5 events were found in the 40 keV unblinded window, resulting in a 27 % probability for the minimum model prediction of 3.5 events and a 41 % probability for the maximum model prediction of 4.2 events. For the *SUM-bege* data set there is a perfect agreement between the observed two events and the expectation of 2.2 events from the model.

If the additional events seen in the 30 keV unblinded window are included to the interpolation the expected BI at  $Q_{\beta\beta}$

increases to  $19 \times 10^{-3}$  cts/(keV kg yr) for the *GOLD-coax* data set.

### 8.2 Sensitivity for GERDA Phase I

Given, for the *GOLD-coax* data set, the background prediction of the minimum model of  $18.5 \times 10^{-3}$  cts/(keV kg yr) and the known GERDA 17.90 kg yr exposure at the end of Phase I, the sensitivity for the  $0\nu\beta\beta$  decay half life  $T_{1/2}^{0\nu}$  was calculated. The value of the exposure-averaged total efficiency (see Eq. 1) for the *GOLD-coax* data set is  $\langle \epsilon \rangle = 0.688$ .

From the energy spectrum an upper limit on the  $0\nu\beta\beta$  signal strength  $N_{up}$  at specified probability or confidence level can be derived and converted to a half life limit  $T_{1/2}^{0\nu}$  using

$$T_{1/2}^{0\nu} > \frac{\ln 2 \cdot N_A}{m_{enr}} \frac{\mathcal{E}}{N_{up}} \langle \epsilon \rangle. \tag{10}$$

In order to estimate the limit setting sensitivity without pulse shape analysis,  $10^4$  MC realizations of GERDA were generated assuming no  $0\nu\beta\beta$  signal. For each realization, the number of events was allowed to fluctuate according to a Poisson distribution with expectation given by the number of predicted background events.

**Fig. 16** Experimental spectrum with minimum (*upper plot*) and maximum (*lower plot*) models around  $Q_{\beta\beta}$  for the *GOLD-coax* data set. The *upper panels* show the individual contributions of the considered background sources to the total background spectrum in logarithmic scale. The *lower panels* show the best fit models fitted with a constant. In the fit the peak areas predicted by the model and the 40 keV blinding window are not considered. The *light grey shaded* (unblinded data, UB data) events in the experimental spectrum have not been used in the analysis

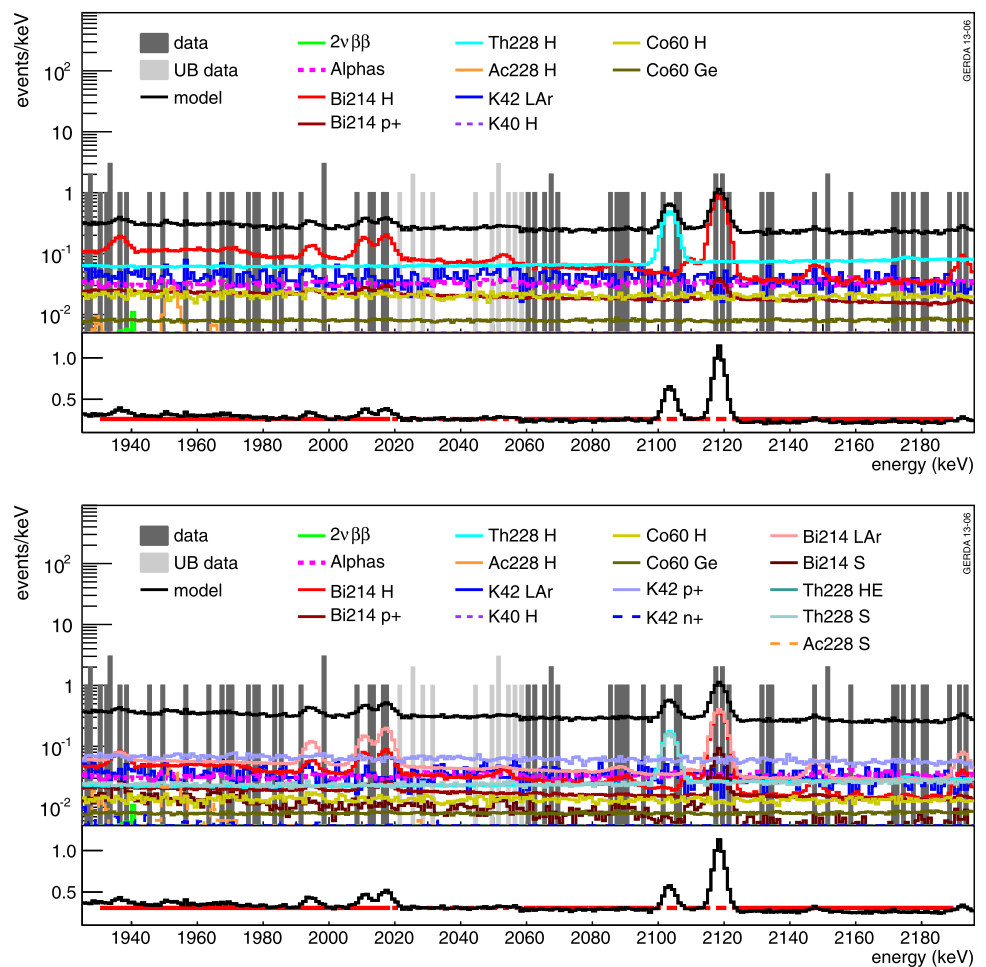


**Table 11** BI in the RoI as predicted by the minimum and maximum models as well as by interpolation from a 200 keV wide window around  $Q_{\beta\beta}$ . Comparison of counts in the previously blinded window (width differs for different data sets) and model predictions is also given. Values in the parentheses show the uncertainty interval

	<i>GOLD-coax</i>	<i>GOLD-nat</i>	<i>SUM-bege</i>
BI in central region around $Q_{\beta\beta}$ (10 keV for coaxial, 8 keV for BEGe)			
$10^{-3}$ cts/(kg keV yr)			
Interpolation	17.5 [15.1, 20.1]	30.4 [23.7, 38.4]	36.1 [26.4, 49.3]
Minimum	18.5 [17.6, 19.3]	29.6 [27.1, 32.7]	38.1 [32.2, 43.3]
Maximum	21.9 [20.7, 23.8]	37.1 [32.2, 39.2]	
	<i>GOLD-coax</i> 30 keV	<i>GOLD-nat</i> 40 keV	<i>SUM-bege</i> 32 keV
Background counts in the previously blinded energy region			
Data	13	5	2
Minimum	8.6 [8.2, 9.1]	3.5 [3.2, 3.8]	2.2 [1.9, 2.5]
Maximum	10.3 [9.7, 11.1]	4.2 [3.8, 4.6]	

The expected lower limit for  $T_{1/2}^{0\nu}$  was estimated by using both, Bayesian and Frequentist analyses. In both analyses the signal and background strengths were free parameters. For the Frequentist analysis, the  $0\nu\beta\beta$  decay rates were estimated from a profile likelihood fit to the unbinned energy spectrum of each realization. The 90 % C.L. lower limit  $T_{1/2}^{0\nu} > 1.9 \times 10^{25}$  yr (90 % C.L.) corresponds to the median

of the 90 % quantile of the profile likelihood. In the Bayesian analysis, the 90 % probability lower limit for  $T_{1/2}^{0\nu}$  was calculated as the median of the 90 % quantiles of the posterior marginalized probabilities  $p(T_{1/2}^{0\nu} | \text{spectrum}, \bar{H})$ , where  $\bar{H}$  is the hypothesis that both background and  $0\nu\beta\beta$  events contribute to the spectrum. The result is  $T_{1/2}^{0\nu} > 1.7 \times 10^{25}$  yr (90 % C.L.). The difference in the numerical values from the

Bayesian and Frequentist analysis (which have conceptually a different meaning) is mainly due to the behavior of the two approaches in the cases when the number of observed counts is smaller than the background expectation. The GERDA sensitivity is expected to be about 10 % better than calculated from the *GOLD-coax* data set only, because of the extra exposure available in the *SILVER-coax* and *SUM-bege* data sets. Also the sensitivity might further increase by applying pulse shape discrimination techniques to the *GOLD-coax*, *SILVER-coax* and *SUM-bege* data sets [10].

## 9 Conclusions

The background measured by the GERDA experiment has been presented in an energy range between 100 and 7500 keV. It has been demonstrated that stable low background data taking with the innovative technique of operating bare HPGe detectors in a cryogenic liquid is possible over a time period of about 1.5 yr. More than 20 kg yr of data have been acquired by the GERDA experiment with six enriched coaxial detectors of a total mass of 14.6 kg and with four enriched BEGe detectors of a total mass of 3.0 kg. A background model has been developed with the  $\Delta E = 40$  keV blinded that allows to predict the BI in this energy range. The predictions of the models have been tested for consistency on a 30 keV (32 keV) range for the coaxial (BEGe) detectors, while the central  $\Delta E = 10$  keV region of interest and  $\Delta E = 8$  keV region for the BEGe detectors around  $Q_{\beta\beta}$  was still blinded. The model describes the background in an energy range from 570 to 7500 keV well. The only significant background contributions in GERDA originate from decays of  $^{42}\text{K}$  in the LAr bath, from  $^{214}\text{Bi}$  in the detector assembly, from residual  $^{222}\text{Rn}$  dissolved in LAr, from  $^{228}\text{Th}$  and  $^{60}\text{Co}$  in the detector assembly, and from surface  $\alpha$  particles. The largest contributions come from contaminants located close to the detectors. Several cross checks confirm the validity of the background model. The 68 % credibility intervals of the BI expected due to the minimum and maximum models at  $Q_{\beta\beta}$  of  $^{76}\text{Ge}$  span the range between 17.6 and  $23.8 \times 10^{-3}$  cts/(keV kg yr). This range includes the systematic uncertainty due to different source location assumptions.

Predictions for the number of events in the blinded region around  $Q_{\beta\beta}$  have been made. It could be shown that the expected background is flat in a region of  $\approx 200$  keV around  $Q_{\beta\beta}$  and that no significant peak like structures are expected in the blinded energy region. The background model and an interpolation of a fit to data from a 200 keV energy window into the blinded energy window give compatible results.

The BI interpolated into the region of interest are  $(1.75_{-0.24}^{+0.26}) \times 10^{-2}$  cts/(keV kg yr) for the coaxial detectors and  $(3.6_{-1.0}^{+1.3}) \times 10^{-2}$  cts/(keV kg yr) for the BEGe detectors.

The statistical uncertainty on the BI prediction from interpolation is of the same size as the systematic uncertainty from the choice of the background model.

The BI obtained from interpolation of the spectrum in a 200 keV window around  $Q_{\beta\beta}$  will be used in the  $0\nu\beta\beta$  analysis of the Phase I data. Given the expected background rate without pulse shape discrimination and assuming no signal, the sensitivity for the *GOLD-coax* data set is  $T_{1/2}^{0\nu} > 1.9 \times 10^{25}$  yr (90 % C.L.) using a profile likelihood fit and  $T_{1/2}^{0\nu} > 1.7 \times 10^{25}$  yr (90 % C.I.) using a Bayesian analysis.

**Acknowledgments** The GERDA experiment is supported financially by the German Federal Ministry for Education and Research (BMBF), the German Research Foundation (DFG) via the Excellence Cluster Universe, the Italian Istituto Nazionale di Fisica Nucleare (INFN), the Max Planck Society (MPG), the Polish National Science Centre (NCN), the Foundation for Polish Science (MPD programme), the Russian Foundation for Basic Research, and the Swiss National Science Foundation (SNF). The institutions acknowledge also internal financial support. The GERDA collaboration thanks the directors and the staff of the LNGS for their continuous strong support of the GERDA experiment.

**Open Access** This article is distributed under the terms of the Creative Commons Attribution License which permits any use, distribution, and reproduction in any medium, provided the original author(s) and the source are credited.

Funded by SCOAP<sup>3</sup> / License Version CC BY 4.0.

## References

1. Particle Data Group, Review of Particle Physics, K. Nakamura et al., *J. Phys. G* **37**, 631 (2010)
2. K.H. Ackermann et al., *Eur. J. Phys. C* **73**, 2330 (2013)
3. G. Douysset, T. Fritioff, C. Carlberg, *Phys. Rev. Lett.* **86**, 4259 (2001)
4. HDM-collaboration: H.V. Klapdor-Kleingrothaus et al., *Eur. Phys. J. A* **12**, 147 (2001)
5. IGEX Collaboration: C.E. Aalseth et al., *Phys. Rev. D* **65**, 092007 (2002)
6. H.V. Klapdor-Kleingrothaus et al., *Phys. Lett. B* **586**, 198 (2004)
7. H.V. Klapdor-Kleingrothaus, I.V. Krivosheina, *Mod. Phys. Lett. A* **21**, 1547 (2006)
8. B. Schwingenheuer, *Annalen der Physik* **525**, 269 (2013)
9. G. Heusser, *Annu. Rev. Part. Nucl. Sci.* **45**, 543 (1995)
10. The GERDA collaboration, M. Agostini et al., *Eur. Phys. J. C* **73**, 2583 (2013)
11. M. Bernabé Heider, PhD thesis, University of Heidelberg (2009)
12. G. Zuzel, H. Simgen, *Appl. Rad. Isot.* **67**, 889 (2009)
13. D. Lenz, PhD thesis, Technical University Munich (2008)
14. I. Barabanov et al., *Nucl. Instr. Methods A* **606**, 790 (2009)
15. L. Pandola et al., *Nucl. Instr. Methods A* **570**, 149 (2007)
16. M. Agostini, L. Pandola, P. Zavarise, *J. Phys. (Conf. Ser.)* **368**, 012047 (2012)
17. P. Zavarise et al., *J. Phys. Conf. Ser.* **375**, 042028 (2012)
18. M. Agostini et al., *JINST* **6**, P08013 (2011)
19. K. Debertin, R.G. Helmer, *Gamma and X-ray Spectroscopy with Semiconductor Detectors* (North Holland, Amsterdam, 1988)
20. GERDA collaboration, M. Agostini et al., *J. Phys. G Nucl. Part. Phys.* **40**, 035110 (2013)



21. N. Becerici-Schmidt for the GERDA collaboration, AIP Conf. Proc. **1549**, 156 (2013). [arXiv:1306.2302](https://arxiv.org/abs/1306.2302)
22. M. Boswell et al., IEEE Trans. Nucl. Sci. **58**, 1212 (2011)
23. GEANT collaboration, S. Agostinelli et al., Nucl. Instr. Methods A **506**, 250 (2003)
24. J. Allison et al., IEEE Trans. Nucl. Sci. **53**, 270 (2006)
25. G. Meierhofer et al., Eur. Phys. J. A **48**, 20 (2012). (and references therein)
26. D.M. Mei et al., Phys. Rev. C **77**, 054614 (2008)
27. I. Barabanov et al., Nucl. Instr. Methods B **251**, 115 (2006)
28. O.A. Ponkratenko, V.I. Tretyak, Yu.G. Zdesenko, Phys. Atom. Nucl. **63**, 1282 (2000)
29. A. Caldwell, D. Kollar, K. Kröninger, Comput. Phys. Commun. **180**, 2197 (2009)
30. R. Aggarwal, A. Caldwell, Eur. Phys. J. Plus **127**, 24 (2012)
31. V.D. Ashitkov et al., Nucl. Instr. Methods A **416**, 179 (1998)
32. E. Aguayo et al., Nucl. Instr. Methods A **701**, 176 (2013)
33. P. Benetti et al., Nucl. Instr. Methods A **574**, 83 (2007)
34. M. Agostini, PhD thesis, Technical University Munich (2013)